Sensing low intracellular potassium by NLRP3 results in a stable open structure that promotes inflammasome activation

Ana Tapia-Abellán[1,2*], Diego Angosto-Bazarra[1*], Cristina Alarcón-Vila[1], María C. Baños[1], Iva Hafner-Bratkovič[3], Baldomero Oliva[4] and Pablo Pelegrín[1,5]

[1]Instituto Murciano de Investigación Biosanitaria IMIB-Arrixaca, Hospital Clínico Universitario Virgen de la Arrixaca, 30120 Murcia, Spain.

[2]Interfaculty Institute for Cell Biology, Department of Immunology, University of Tübingen, Auf der Morgenstelle 15, 72076 Tübingen, Germany.

[3]Department of Synthetic Biology and Immunology, National Institute of Chemistry, Ljubljana, Slovenia; EN-FIST Centre of Excellence, Ljubljana, Slovenia.

[4]Laboratory of Structural Bioinformatics (GRIB), Department of Experimental and Health Sciences, Universitat Pompeu Fabra, Barcelona, 08003, Spain.

[5]Department of Biochemistry and Molecular Biology B and Immunology, Faculty of Medicine, University of Murcia, 30120 Murcia, Spain.

*These authors contributed equally to this work.

Corresponding author: Dr. Pablo Pelegrín. Edificio LAIB 4ª Planta, Instituto Murciano de Investigación Biosanitaria (IMIB-Arrixaca). Carretera Buenavista s/n. 30120 El Palmar, Murcia, Spain. Phone: +34 868 885 038; e-mail: pablo.pelegrin@imib.es

SHORT TITLE: Structural sensing of K^+ efflux by NLRP3.

ONE-SENTENCE SUMMARY: The specific NLRP3 N-terminal domain is essential for NLRP3 activation and inflammasome formation in response to K^+ efflux.

ABSTRACT

The NLRP3 inflammasome is activated in response to a wide range of stimuli and drives diverse inflammatory diseases. The decrease of intracellular K^+ concentration is a minimal upstream signal to most of the different NLRP3 activation models. Here we found that cellular K^+ efflux induces a stable structural change in the inactive NLRP3 promoting an open conformation as a step preceding activation. This conformational change is facilitated by the presence of the specific NLRP3 FISNA domain and a unique flexible linker sequence between the PYD and FISNA domains. This linker is also important to facilitate the ensemble of $NLRP3^{PYD}$ into a seed structure for ASC oligomerization. The introduction of the NLRP3 PYD-linker-FISNA sequence into NLRP6 resulted in a chimeric receptor able to be activated by K^+ efflux-specific NLRP3 activators and promoted an *in vivo* inflammatory response to uric acid crystals. Our results establish that the N-terminal sequence between PYD and NACHT domain of NLRP3 is key for inflammasome activation.

INTRODUCTION

NLRP3 forms a unique inflammasome because it can be activated in response to many different and exclusive stimuli, most of them are sterile damage-associated molecular patterns (DAMPs) from the host (1, 2). This implicates NLRP3 in the pathophysiology of different chronic inflammatory diseases that are not driven by infections, as well as, in metabolic and neurodegenerative diseases (2). The different NLRP3 activating stimuli converge in the interaction of NLRP3 with several accessory molecules to facilitate its activation. These molecules include, among others, the protein never in mitosis A-related kinase 7 (NEK7), the thioredoxin-interacting protein (TXNIP), the microtubule-affinity regulating kinase 4 (MARK4), the stress granule DEAD box helicase 3 X-linked protein (DDX3X), the mitochondrial antiviral-signaling protein (MAVS) and the receptor for activated protein C kinase 1 (RACK1), as well as exposed cardiolipin in mitochondria or phosphatidylinositol-4-phosphate (PtdIns4P) in dispersed trans Golgi network (*3*–*9*). However, the decrease of intracellular K^+ is a common minimal cellular step for the majority of NLRP3 stimuli (*10*, *11*), being the interaction of NLRP3 with NEK7 or with PtdIns4P in dispersed trans Golgi network dependent on intracellular K^+ efflux (3, 4). However, how a decrease in the intracellular K^+ concentration, a key common step for NLRP3 activation (*12*), favors NLRP3 inflammasome assembly remains unknown. After activation, NLRP3 homo-oligomerizes forming a multimeric structure that recruits the adaptor protein ASC (*13*), and then ASC molecules form large filaments by subsequent ASC^{PYD}-ASC^{PYD} homotypic interactions (*14*). Then, ASC filaments form a single large structure (called ASC 'speck'), that recruits and activates caspase-1 (*15*, *16*). Active caspase-1 controls downstream inflammasome signaling executing the processing of pro-inflammatory cytokines, such as interleukin (IL)-1β, and gasdermin D a protein inducing pyroptotic cell death (*17*). Pyroptosis also allows the release of ASC specks amplifying the inflammatory response and provoking among other effects, amyloid deposition (*18*–*20*).

In this study, by using a bioluminescence resonance energy transfer (BRET) technique to monitor NLRP3 conformational changes, we have identified that the specific N-terminal NLRP3 linker and FISNA domain are key to provoke a stable change on the inactive NLRP3 structure after a decrease of intracellular K^+ concentration, allowing activation of NLRP3. The sequence between the PYD and FISNA domains should probably be a flexible linker that also favors the correct placement of $NLRP3^{PYD}$ to engage ASC into the inflammasome. However, this linker sequence is dispensable for K^+-efflux dependent NLRP3 structural change and oligomerization, as NLRP3 with deletions of this region are activated in a K^+-efflux dependent manner. NLRP6 harboring the NLRP3 PYD-linker-FISNA sequence is able to form a functional inflammasome in response to K^+ efflux, and drives an *in vivo* immune response in the NLRP3-specific uric acid crystal model. These different unique structural features of NLRP3 involved in this response can explain why only NLRP3 and no other NLRs can be activated in response to intracellular K^+ decrease.

RESULTS

NLRP3 structure is modified by intracellular K^+ efflux

LPS-primed mouse macrophages treated with increased concentrations of the K^+ ionophore nigericin, dose-dependently decreased intracellular K^+ concentration and in parallel increased IL-1β release (calculated IC_{50} of 0.8 μM and 1.5 μM respectively) (**Fig. 1A**). Similarly, other two K^+ ionophores, valinomycin and BB15C1, were also able to induce IL-1β release with a parallel decrease of intracellular K^+ concentration (**Fig. S1**). Nigericin-induced IL-1β release was dose-dependently inhibited by increasing concentrations of extracellular KCl, with an IC_{50} of 16 mM (**Fig. 1B**). To rule out unspecific effects of the increase of extracellular K^+ concentrations, we used extracellular Rb^+, a slightly larger metal ion analogue to K^+ that mimics a lower K^+ conductance in most ion channels and ionophores. We found that extracellular RbCl, but not CsCl or LiCl (ions that do not permeate through K^+-selective pores), blocked IL-1β release induced by nigericin, without significantly impairing IL-1β release associated to the K^+-insensitive Pyrin inflammasome activated by *C. difficile* toxin B (TcdB) (**Fig. 1C**). These results and previous data (*12*, *21*), confirm that a decrease of intracellular K^+ is linked to the activation of the NLRP3 inflammasome. To gain insight on how the decrease in intracellular K^+ could activate NLRP3, we used HEK293T cells as a validated cellular model to study NLRP3 oligomerization and activation (*4*, *22*–*24*). We found that nigericin treatment induced NLRP3 oligomerization, being this oligomerization blocked by extracellular KCl (**Fig. 1D**). NLRP3 oligomers induced by nigericin in HEK293T cells colocalize with ASC specks (when ASC was co-expressed together NLRP3), similarly to when NLRP3 is activated in macrophages (**Fig. 1E**), suggesting that the NLRP3 oligomers found in HEK293T cells after nigericin treatment present a functional structure. We next used an NLRP3 BRET sensor expressed in HEK293T cells (*22*, *25*), and found that nigericin induced a decrease of the BRET signal for NLRP3 that was stable for up to 1.5 h after stimulation (**Fig. 2A**). Increasing extracellular KCl concentration impaired

nigericin-induced NLRP3 BRET signal change (**Fig. 2A**), indicating that K^+ efflux could stably change the structure of NLRP3. The structural change induced by nigericin in NLRP3 was dose-dependently inhibited by increasing concentrations of extracellular KCl with an IC_{50} of 43 mM (**Fig. 2B**). Extracellular Rb^+-based buffer, but not a Li^+-based buffer, also blocked the stable NLRP3 BRET signal decrease induced by nigericin (**Fig. 2C**). The use of valinomycin and BB15C1 K^+ ionophores, as well as the activation of P2X7 receptor with ATP (in HEK293T cells expressing P2X7), resulted in a stable decrease of NLRP3 BRET signal that was impaired when the extracellular solution contained elevated concentration of KCl (**Fig. 2D**). The decrease of the NLRP3 BRET signal has been recently reported to be a transient intermediate NLRP3 structure with an open conformation that promotes activation (*22*), indicating that intracellular K^+-efflux could open NLRP3 structure favoring its oligomerization. In the absence of a full length NLRP3 structure in inactive and active conformation it is difficult to precisely interpret the change in BRET signal. Our previous studies demonstrated that upon NLRP3 triggering, the NLRP3 BRET signal is reduced and that NLRP3 with CAPS-related mutants have lower resting BRET signals (*9*, *24–27*), indicating a distancing of luciferase and YFP epitopes by an opening of the NLRP3 structure. Therefore, we modeled a semi-open and an open NLRP3 conformation based on the recent NLRP3 structure (6NPY) and the structure of NLRC4 inside an oligomer (3JBL) (*28*, *29*), and we found that structurally a hinge that allowed this conformational change was on the NACHT domain (residues 417-441 inside the HD1 motif, **Fig. S2A**). This hinge was able to move in block a compact helix bundle of the NACHT domain and was conserved in the NACHT of other NLRs, as NLRP6 (**Fig. S2A**). By analyzing NLRP3 structures, we found that in the semi-activated not fully open structure (6NPY) the nucleotide binding pocket was hidden and would prevent ATP entry (**Fig. S2B**). On the contrary, the open NLRP3 structure presents an accessible nucleotide binding pocket that could allow exchange of nucleotides and the entry of ATP (**Fig. S2B**). Since ATP hydrolysis is important for NLRP3 activation (*30*), our data support

that the conformational opening of NLRP3 structure would favor ATP entry and further NLRP3 activation.

NLRP3^{PYD} is dispensable for NLRP3 oligomerization, but is necessary to form active NLRP3 oligomers

We recently demonstrated that the LRR domain of NLRP3 is not a repressor domain and is dispensable for NLRP3 activation (*31*), this led us to study if the N-terminal domain could have a role in the activation of NLRP3. NLRP3 lacking the PYD N-terminal domain (ΔPYD-NLRP3, Δ1-91) was able to oligomerize after nigericin stimulation (**Fig. 3A**) and to reduce the BRET signal similar to the one observed in NLRP3 wild-type after nigericin treatment (**Fig. 2A,3B**). ΔPYD-NLRP3 BRET signal was intramolecular (**Fig. S3A**), similarly to the full-length NLRP3 (*22*, *25*). Oligomerization and the decrease of the ΔPYD-NLRP3 BRET signal induced by nigericin, was blocked using an extracellular buffer with elevated KCl concentration (**Fig. 3A,B**), demonstrating that the PYD domain is not necessary for NLRP3 oligomerization in response to intracellular K^+-efflux. However, ΔPYD-NLRP3 expressed in NLRP3-deficient macrophages (**Fig. S3B**) was unable to induce the release of IL-1β after nigericin activation (**Fig. 3C**), as it could not bind to ASC (**Fig. 3D**). Therefore, the PYD domain is not necessary for NLRP3 oligomerization, suggesting that is not the trigger-sensing domain, but is crucial to form fully functional NLRP3 oligomers by allowing the recruitment of ASC.

The NLRP3 sequence between the PYD and NACHT is important for inflammasome activation in response to K^+-efflux

Since the PYD domain was not critical for NLRP3 oligomerization in response to K^+ efflux, but was important to engage ASC and form functional inflammasomes, we

decided to model the NLRP3 oligomeric structure including the N-terminal PYD and the sequence up to the NACHT domain. In NLRP3, this sequence is encoded by a specific exon present only in mammalian NLRP3 sequences among all NLRPs (**Fig. S4A-C**), and then is followed by the fish-specific NACHT associated (FISNA) domain (PFAM: PF14484), a domain frequently found in proteins associated with the NACHT domain and only present in two of the human NLRs: NLRP3 and NLRP12 (**Fig. S4C**). NLRP3 modelling was done using the structure of NLRP3 in complex with NEK7 (6NPY) (*28*) and the structure of the $NLRP3^{PYD}$ domain (3QF2) to complete the structure that was optimized to avoid clashes (**Fig. 4A,B**). This model showed that the $NLRP3^{FISNA}$ domains were actually interacting between NLRP3 monomers inside the oligomer (**Fig. 4A,B**). The sequence encoded by the NLRP3 exon 3 (residues 92-132) appeared as a linker formed by an α-helix and a flexible sequence that is able to position the PYD domains of the different NLRP3 subunits in a compatible conformation with the assembly of ASC^{PYD} domains forming an helical fiber (**Fig. 4A,B**). At the end of the α-helix of the linker there is a polybasic sequence ($KMKK^{132}$) associated with NLRP3 activation, as it mediates the binding of NLRP3 to negatively charged phospholipids, as PtdIns4P in the dispersed trans Golgi network, a phenomenon occurring by a stimulus-specific mechanism (*4*). Our model predicts that these positively charged residues, together with the positive residues at the beginning of the FISNA domain ($RKKYRKYVRSR^{145}$) (**Fig. S5**), allow the linker α-helix to position the PYD domain nearer or farther the FISNA domain in the oligomeric structure, placing it in an oligomeric helix and creating a seed for ASC^{PYD} nucleation (**Fig. 4A**). Based on this model, we would expect that the removal of the NLRP3 linker sequence would decrease the engagement of ASC, meanwhile the lack of the FISNA domain would dramatically affect NLRP3 oligomerization.

Indeed, in *Nlrp3*$^{-/-}$ macrophages, expression of NLRP3 serial truncations of the sequence between the PYD and NACHT domain, maintaining the PYD domain (**Fig. S4A**), confirmed a progressive lack of activity as denoted by a decrease of IL-1β release

induced by nigericin (**Fig. 5A**). Although the release of IL-1β induced by nigericin was reduced when macrophages expressed NLRP3 Δ92-120 and Δ92-132 (lacking partially or totally the linker sequence), it was blocked when nigericin was added in an extracellular buffer with an elevated KCl concentration (**Fig. 5A**). Expression of NLRP3 truncations getting into the FISNA domain (Δ92-148) or deleting the middle or final sequence of the FISNA domain (Δ149-180 or Δ181-217), or complete sequence between PYD and NACHT (Δ92-217) resulted in a receptor that was unable to induce IL-1β release after nigericin stimulation (**Fig. 5A, S6A**). In fact, the expression of NLRP3 Δ92-120 in *Nlrp3*$^{-/-}$ macrophages resulted in nigericin induced activation of caspase-1 and processing of IL-1β and GSDMD (**Fig. 5B**). The specific NLRP3 inhibitor MCC950 was able to block caspase-1 activation and IL-1β release by NLRP3 Δ92-120 activation (**Fig. 5B**), confirming that this NLRP3 truncation presented a canonical NLRP3 activation, since the target sequence for MCC950 relays on the NLRP3^{NACHT} domain (*22*, *32*). In contrast, these macrophages expressing different NLRP3 truncations released similar concentrations of IL-1β when the Pyrin inflammasome was activated (**Fig. S6B**) and similar concentrations of IL-6 after LPS priming (**Fig. S6C**). Our NLRP3 structural modeling predicts that the linker sequence is required to position NLRP3^{PYD} in an optimal helical filament that will seed and nucleate ASC^{PYD}, but not to stabilize NLRP3 oligomers (**Fig. 4A,B**). We confirmed that macrophages expressing NLRP3 Δ92-120 and Δ92-132 (lacking partially or totally the linker sequence) were able to increase the percentage of cells with ASC specks when treated with nigericin, but this increase was highly reduced when NLRP3 Δ92-132 was expressed and completely absent when NLRP3 Δ92-148 was expressed (**Fig. 5C,D**). We then studied oligomerization of NLRP3 Δ92-120, Δ92-132 and Δ92-148 truncations when expressed in HEK293T cells (lacking ASC expression). Both NLRP3 Δ92-120 and Δ92-132 truncations, but not the Δ92-148 truncation, were able to oligomerize after nigericin stimulation (**Fig. 5D**). As our model predicted (**Fig. 4A**), in macrophages expressing the NLRP3 Δ92-132 truncation, several NLRP3 oligomers

were not co-localizing with the ASC specks (**Fig. 5D**). These data support the idea that the FISNA domain would be important for NLRP3 oligomerization in response to nigericin. However, the linker sequence could be important to allow an optimal engagement of ASC to the NLRP3 oligomers. Truncation of the linker sequence (92-132) resulted in a less flexible linker, that did not affect NLRP3 oligomerization upon K^+-efflux. We next found out that the expression of NLRP3 BRET sensor carrying different deletions in the region between PYD and NACHT domain in HEK293T cells resulted in an intramolecular BRET signal (**Fig. S6D,E**). Nigericin induced a K^+-efflux dependent stable reduction of NLRP3 BRET signal for Δ92-120 and Δ92-132 deletions, but not for Δ92-148 (**Fig. 5E**). The BRET signal from different deletions of the FISNA sequence (Δ149-180 and Δ181-217), that failed to induce IL-1β release in response to nigericin (**Fig. S6A**), was also not affected by nigericin (**Fig. 5F**). Moreover, the reduction of NLRP3 Δ92-132 BRET signal induced by nigericin, was reverted in the presence of MCC950 (**Fig. 5E**), similarly to the effect of this compound on the full-length NLRP3 BRET signal (*22*). This further support that the stable reduction of NLRP3 BRET signal lacking the linker sequence reflect an open active NLRP3 conformation. The fact that human NLRP3 Δ92-132 was still able to respond to K^+ efflux induced by nigericin could suggest that the identified polybasic sequence in the mouse NLRP3 sequence ($KKKK^{130}$) important for activation (*4*) might be functioning differentially in the human NLRP3. In fact, specific mutations of the $KMKK^{132}$ polybasic sequence of human NLRP3 to $AMAA^{132}$ released similar IL-1β after nigericin stimulation when compared to NLRP3 wild-type or polybasic $RMRR^{132}$ rescue mutant expressed in macrophages lacking endogenous wild-type NLRP3 (**Fig. S6F**). High extracellular K^+ blocked this activation, and the release of IL-1β dependent on Pyrin inflammasome activation was unaffected by the presence of these mutations (**Fig. S6F**). Furthermore, NLRP3 $AMAA^{132}$ mutant was also able to oligomerize after nigericin treatment when expressed in HEK293 cells in a K^+-efflux dependent manner (**Fig. S6G**). Specific $AMAA^{132}$ mutation in NLRP3 also resulted in a

reduced BRET signal in response to nigericin with a similar profile than wild-type and RMRR^{132} mutant NLRP3 (**Fig. S6H**). These data suggest that binding to PtdIns4P in the dispersed trans-Golgi network in the human NLRP3 by the KMKK^{132} sequence is not as critical as for the mouse NLRP3 with a KKKK^{130} sequence (*4*). This could reflect that the presence of a second polybasic region in the human NLRP3 (RKKYRKYVRSR^{145}) at the beginning of the FISNA domain could be important for human NLRP3 interaction with dispersed trans-Golgi network after K^+-efflux.

NLRP3 PYD-linker-FISNA sequence renders NLRP6 sensitivity to K^+-efflux

To corroborate the structural model data and that the NLRP3 linker-FISNA sequence is important to activate NLRP3 inflammasome in response to K^+-efflux, we constructed chimeric receptors with NLRP6, a receptor that is not activated by K^+-efflux (*33*, *34*). NLRP6 presents a shorter sequence between the PYD and NACHT domains since it lacks the flexible linker sequence coded by the unique NLRP3 exon 3 (**Fig. S7A,B**). Furthermore, NLRP6 does not have a conserved annotated FISNA domain, but presents some conserved features with the NLRP3 FISNA domain, particularly an initial polybasic sequence and some structural motifs, including three putative residues interacting with the nucleotide, with an overall similarity of 46.1% and a 49.3% homology with the FISNA family signature (**Fig. S7B,C**). We first demonstrated that NLRP6 was not endogenously expressed in the *Nlrp3*$^{-/-}$ macrophages used in this study (**Fig. S8A**) and the expression of NLRP6 led to the release of IL-1β induced by lipoteichoic acid (**Fig. S8B**), indicating that NLRP6 when expressed in these macrophages was able to form functional inflammasomes as has been already reported (*33*). We then expressed in *Nlrp3*$^{-/-}$ macrophages NLRP6 containing different lengths of the NLRP3 N-terminal sequence, starting from the NLRP3^{PYD} domain (1-91), the NLRP3^{PYD} and the flexible linker sequence (1-132), and the NLRP3 PYD-linker-FISNA (1-217). Nigericin was not able to

induce the release of IL-1β when macrophages expressed the full-length NLRP6, but the NLRP3/6 chimeric receptors released increased concentrations of IL-1β in response to nigericin when the longer NLRP3 sequence was introduced into the NLRP6 (**Fig. 6A**). However, the K^+-efflux dependence for IL-1β release after nigericin stimulation was clearly observed for the full-length NLRP3 and the chimera NLRP3(1-217)-NLRP6(196-892) (**Fig. 6A**). This data supports the notion that the NLRP3 N-terminal sequence between PYD and NACHT facilitates the formation of functional inflammasomes that promote the recruitment of ASC in response to K^+-efflux. Due to the similarity of NLRP3 FISNA with the NLRP6 sequence between PYD and NACHT (**Fig. S7B**), this last one could be taking a similar conformation and some functionality in sensing K^+-efflux, since NLRP6 also present a polybasic sequence $KKKYREHVLQL^{129}$ (**Fig. S7A,B**) that was present in the chimeras NLRP3(1-91)-NLRP6(104-892) and NLRP3(1-132)-NLRP6(104-892) (**Fig. 6A**). Expression of the different chimeric receptors was not able to affect IL-1β release after Pyrin inflammasome activation or IL-6 release after LPS priming (**Fig. S8C,D**). Furthermore, the chimera NLRP3(1-217)-NLRP6(196-892) was able to activate caspase-1 and process IL-1β in response to nigericin in a caspase-1 dependent manner (**Fig. 6B,C**), but the release of IL-1β induced by nigericin was insensitive to MCC950 (**Fig. 6C**), supporting the idea that this compound specifically targets the $NLRP3^{NACHT}$, but not the $NLRP6^{NACHT}$ domain (*22*, *32*). The chimera NLRP3(1-217)-NLRP6(196-892) was also able to increase the percentage of cells with ASC specks when macrophages *Nlrp3*$^{-/-}$ were activated with nigericin (**Fig. 6D**) and in HEK293T cells in a K^+-efflux dependent manner (**Fig. 6E**). Nigericin was able to induce oligomerization of chimeric NLRP3(1-217)-NLRP6(196-892) when expressed in HEK293T cells without ASC, and the formation of these oligomers were abolished when high extracellular KCl was used (**Fig. 6F**). This suggests that the NLRP3 PYD-linker-FISNA sequence is a key region to induce a conformational change in NLRP3 after K^+ efflux and favor NLRP3 activation.

The NLRP3 N-terminal domain is important for activation in response to crystals

Particulate matter, such MSU crystals, activate NLRP3 by a decrease of the intracellular K^+ concentration (*12*, *35*). However, the kinetics of NLRP3 activation induced by crystals is slower than when K^+-efflux is driven by an ionophore or the activation of ion channels (*36*), probably due to the slow dilution of intracellular K^+ concentration when MSU induces cell swelling (*35*). We found that MSU induced IL-1β release from *Nlrp3*$^{-/-}$ macrophages expressing NLRP3 with the deletion Δ92-120 and much less with the deletion Δ92-132, but not when the deletions Δ92-148 or Δ92-217 were expressed (**Fig. 7A**). High extracellular K^+ was able to significantly reduce IL-1β release induced by NLRP3 Δ92-120 and Δ92-132 (**Fig. 7A**), supporting the data observed with nigericin. The NLRP3 mutant AMAA^{132} was also able to release IL-1β in a K^+-dependent manner upon MSU activation similarly to the polybasic RMRR^{132} mutant (**Fig. S8E**), further supporting that human KMKK^{132} NLRP3 sequence is dispensable for activation. Swapping NLRP6 N-terminus sequence with the NLRP3 sequence resulted in a chimeric receptor that when expressed in *Nlrp3*$^{-/-}$ macrophages released IL-1β after MSU treatment when the NLRP3 sequence included the PYD and the linker sequence (1-132) or the PYD-linker-FISNA (1-217), dependent on K^+-efflux (**Fig. 7B**). These results support that the activation of NLRP3 induced by MSU crystals could also be facilitated by the linker (92-132) sequence.

The linker sequence is important for NLRP3 activation in response to specific K^+-independent NLRP3 stimulus

NLRP3 can be also activated by imiquimod and derivatives in a K^+-efflux independent manner (*37*), and the mouse NLRP3 polybasic sequence KKKK^{130} of the linker domain has been reported as critical for this activation (*4*). Here we found that the human NLRP3 Δ92-120 deletion, but not the Δ92-132, Δ92-148 or Δ92-217 deletions, was able to induce

IL-1β release after imiquimod treatment when expressed in *Nlrp3*$^{-/-}$ macrophages (**Fig. 7C**). Accordingly, IL-1β release induced by imiquimod in NLRP3 Δ92-120 deletion was insensible to K^+-efflux (**Fig. 7C**), indicating that the predicted α-helix of the linker sequence found in 120-132 sequence could be important for K^+-independent stimulation of NLRP3. However, the $KMKK^{132}$ polybasic sequence appears not to be critical for NLRP3 activation in response to imiquimod, as *Nlrp3*$^{-/-}$ macrophages expressing $AMAA^{132}$ NLRP3 mutants were able to release IL-1β in a K^+-independent manner after imiquimod activation (**Fig. S8F**). Furthermore, including NLRP3 PYD-linker (1-132), or NLRP3 PYD-linker-FISNA (1-217) of NLRP3 in NLRP6 background resulted in a chimeric receptor that when expressed in *Nlrp3*$^{-/-}$ macrophages released IL-1β after imiquimod treatment (**Fig. 7D**). In fact, imiquimod was able to induce NLRP3 oligomerization (**Fig. 7E**) and decreased NLRP3 BRET signal (**Fig. 7F**) independently of K^+ efflux. These data support that imiquimod could also induce a conformational change in NLRP3 for activation and that the NLRP3 linker sequence (92-132), and particularly the N-tail of the α-helix, is key to activate NLRP3 in response to imiquimod in a K^+-efflux independent manner.

NLRP6 with the NLRP3 PYD-linker-FISNA sequence induces an inflammatory response *in vivo*

MSU crystals induce inflammation through NLRP3 receptor activation (*38*). In fact, NLRP3 deficient mice present less peritoneal IL-1β and less peritoneal granulocyte infiltration when challenged intraperitoneally with MSU crystals compared to wild-type mice (**Fig. S9A**), being this an established model for NLRP3-driving peritonitis (*38*). We developed a model using *Nlrp3*$^{-/-}$ mice intraperitoneally reconstituted with immortalized *Nlrp3*$^{-/-}$ mouse macrophages expressing either NLRP6, the chimera NLRP3(1-217)-NLRP6(196-892) or NLRP3, and then challenged with intraperitoneal MSU crystals (**Fig.**

8A). These macrophages were present in the peritoneum by the time MSU would be administered and after the final recovery of peritoneal exudates (**Fig. S9B**). The recovered recombinant peritoneal macrophages were functional activating the inflammasome (**Fig. S9C**). MSU crystals induced an increase of IL-1β and IL-18 concentration in the peritoneum of *Nlrp3*$^{-/-}$ mice reconstituted with *Nlrp3*$^{-/-}$ macrophages expressing NLRP3 and the chimera NLRP3(1-217)-NLRP6(196-892), but not when NLRP6 was expressed (**Fig. 8A**). IL-6 concentration in the peritoneum of these mice was very low and similar between the different macrophages reconstituted into the peritoneum (**Fig. S9D**). Mice reconstituted with macrophages with the chimeric NLRP3(1-217)-NLRP6(196-892) and full length NLRP3 receptor, induced an increase of IL-1 dependent chemokines CXCL1, CXCL10 and CCL2 in the peritoneum of mice intraperitoneally injected with MSU crystals (**Fig. 8B**) and with a parallel increase of the percentage of infiltrating granulocytes (**Fig. 8C**). This *in vivo* model indicates that the NLRP3 PYD-linker-FISNA sequence is key to initiate an inflammatory response to MSU crystals.

DISCUSSION

The NLRP3 inflammasome has been implicated in multiple diseases and therefore its activation mechanism involves diverse signalling steps that remain not fully understood. However, the majority of NLRP3 triggers share the requirement to induce a reduction in the intracellular concentration of K^+ (*10*, *11*). In the present study we identified that the inactive NLRP3 protein structure changes to favour activation in response to low concentrations of intracellular K^+. The linker and FISNA domain, a NLRP3-specific domain, both located between the N-terminal PYD and central NACHT domains, are important to activate NLRP3 when intracellular K^+ decreases and also when K^+-independent activators are used. The notion that the LRR domain of NLRP3 could be responsible for a ligand-binding activation model, has been recently challenged by the identification of a minimal NLRP3 sequence lacking the LRR that is activated in a K^+-efflux dependent manner similarly to the full-length NLRP3 (*31*). Our results support this model as we identified the region between the PYD and NACHT domains as critical for NLRP3 activation. The interaction of mouse NLRP3 with negatively charged lipids in the dispersed trans-Golgi network by a polybasic sequence present in the region between the NLRP3 PYD and NACHT domain ($KKKK^{130}$) at the end of exon 3, is important for its activation (*4*). However, while the dispersion of trans-Golgi network induced by the different NLRP3 activators is independent of K^+-efflux, the activation of NLRP3 is blocked by increasing extracellular concentrations of KCl and therefore dependent on the efflux of K^+ (*4*, *12*). To avoid possible artefacts of the use of elevated concentrations of extracellular KCl, we also found that NLRP3 is equally blocked by increasing extracellular RbCl, being Rb^+ mimicking K^+ conductance in most K^+ permeable channels and ionophores. Our data indicate that the decrease of intracellular K^+ concentration changes the inactive structure of NLRP3, resulting in a conformation favouring the functional oligomerization of the receptor into active oligomers. This conformational change is independent of the partially conserved polybasic region of mouse NLRP3 that binds to PtdIns4P ($KKKK^{130}$), as the human NLRP3 ($KMKK^{132}$) mutant lacking this region (Δ92-

132) or the AMAA^{132} mutant were still undergoing the same conformational change as measured by a reduction of the BRET signal. Although in the absence of a full length NLRP3 structure in active conformation it is difficult to interpret the change in BRET signal, it suggests that either a conformational change occurs before NLRP3 binding to negatively charged lipids on the dispersed trans-Golgi network or that an additional polybasic sequence found at the beginning of the FISNA domain in the human NLRP3 (RKKYRKYVRSR^{145}) could be important for PtdIns4P binding in the dispersed trans-Golgi network allowing then a conformational change of the receptor. In fact, additional deletion of this second polybasic region in NLRP3 (Δ92-148) completely prevents NLRP3 activation and probably recruitment to the dispersed trans-Golgi network, as this second polybasic sequence was also important for mouse NLRP3 binding to PtdIns4P (*4*). After NLRP3 binding to the dispersed trans-Golgi network, the receptor is trafficked to the centrosome for full inflammasome activation, where it probably facilitates its interaction with the centrosome-localized kinase NEK7 and the adaptor protein ASC (*39*). Consistent with our study, the interaction of NEK7 with NLRP3 occurs after K^+ efflux (*3*). A incomplete NLRP3 structure bound to NEK7 has been solved (*28*), this NLRP3 structure is partially closed and is considered a semi-inactive NLRP3. We found that the NLRP3 nucleotide binding site in this NLRP3/NEK7 structure is locked, impeding the exchange of ADP for ATP, which is also required for NLRP3 activation (*30*). Therefore the opening of the NLRP3 inactive structure induced by K^+ efflux could facilitate the entrance of ATP to the nucleotide binding pocket and NLRP3 activation. In fact, during cell swelling, the decrease of intracellular K^+ is responsible for a conformational change in the inactive NLRP3 molecules existing in pre-assembled inactive complexes (*24*). Our present study indicates, using an intra-molecular BRET sensors, that the NLRP3 conformational change during activation is dependent on the presence of the FISNA domain that includes a second polybasic sequence (RKKYRKYVRSR^{145}) possibly important for human NLRP3 binding to PtdIns4P and activation. Further, the linker sequence between the PYD and FISNA (92-132) may assist on the correct placement of

the NLRP3^{PYD} domain to form a seed for ASC^{PYD} nucleation, thus supporting active oligomer formation. Therefore, the NLRP3 N-terminal sequence is important for NLRP3 inflammasome activation in response to K^+ efflux.

Imiquimod and derivatives are activators of the NLRP3 inflammasome (*40*), but their mechanism of activation is independent of K^+ efflux (*37*) and dependent on the binding of NLRP3 to PtdIns4P in the dispersed trans-Golgi network (*4*). Our study demonstrates that imiquimod is also able to induce a decrease of NLRP3 BRET signal, suggesting a similar conformational change on NLRP3 than when nigericin is applicated and probably favouring the activation of the inflammasome. We found that the presence of the linker sequence (92-132), between the PYD and FISNA domain, is important for NLRP3 activation by imiquimod, indicating that both K^+-dependent and -independent activation of NLRP3 would share a similar conformational change involving a specific N-terminal domain on the receptor, since both types of triggers induce a reduction in the NLRP3 BRET signal. In fact, we also previously reported a decrease of the NLRP3 BRET signal in active NLRP3 mutants associated to autoinflammatory syndromes (*22*).

The NLRP6 inflammasome is triggered by some Gram-positive bacteria cell wall polymers such as lipoteichoic acid (*33*), however it cannot be activated by classical NLRP3 triggers that induce K^+ efflux (*34*). Therefore, NLRP3 is unique among other inflammasome sensors since it is the only one able to respond to specific damage- and homeostasis-associated molecular patterns. By introducing the N-terminal fragment of NLRP3 in NLRP6, we generated a chimeric receptor that is activated in response to nigericin, MSU crystals and imiquimod. Therefore, the N-terminal sequence of NLRP3 is key for its activation in response to specific triggers, except for the PYD domain that is not necessary for NLRP3 activation and oligomerization, but is crucial to create functional NLRP3 inflammasome by allowing the recruitment of ASC (*13*). The NLRP3 inhibitor MCC950 specifically binds to the NACHT domain of NLRP3 and affects the active structure of NLRP3 (*22*, *32*), and here we found that MCC950 is not blocking the chimeric

NLRP3/NLRP6 receptor, further supporting the specificity of MCC950 over NLRP3 NACHT domain.

Altogether, these results reveal that the NLRP3 sequence between the PYD and NACHT is important to confer responsiveness of NLRP3 to specific triggers. Therefore, the unique ability of NLRP3 to activate in response to signals that decrease intracellular K^+ resides in the presence of a linker sequence encoded by a specific NLRP3 exon 3 and the FISNA domain, which are necessary to facilitate a structural change of the closed inactive NLRP3 protein. Then, the linker sequence is also important to activate NLRP3 in response to K^+-independent triggers, and facilitates an optimal orientation of the $NLRP3^{PYD}$ domain within the active NLRP3 oligomer to form a helical seed to interact with ASC^{PYD} and form a fully active inflammasome.

MATERIALS & METHODS

Plasmid construction. The different constructs of human NLRP3 and NLRP6 were generated by overlapping PCR (Uniprot #Q96P20 and #P59044 annotations for human NLRP3 and NLRP6 respectively) and cloned into pcDNA3.1/V5-His TOPO (Life Technologies). Sequencing of all constructs was performed to confirm correct modification and the absence of unwanted mutations. All constructs were designed to contain YFP at the N-terminus for microscopy assays or double tagged with YFP at the N-terminus and Renilla Luciferase (Luc) at the C-terminus to generate the various BRET sensors. NLRP3 containing Renilla Luciferase (Luc) at the C-terminus were also constructed in pcDNA3.1/V5-His TOPO, sequenced to confirm correct alignment between the tag and the NLRP3 sequence, and were used as controls in all BRET assays.

Cells and transfections. HEK293T cells (CRL-11268; American Type Culture Collection) were maintained in DMEM/F12 (1:1) (Lonza) supplemented with 10% fetal calf serum (FCS) (Life Technologies), 2 mM Glutamax (Life Technologies) and 1% penicillin-streptomycin (Life Technologies). HEK293T cells stably expressing the rat P2X7 receptor have previously been described (*41*) and were cultured in F-12 media (Lonza) supplemented with 10% FCS. Lipofectamine 2000 was used for the transfection of HEK293T cells according to the manufacturer's instructions. After two days of transfection, stable selection of HEK293T clones expressing the different NLRP3 constructs was initiated by supplementing cell culture media with G418 (2 mg/ml, Acros Organic). After 4 weeks of culture in G418, cell cloning was performed by serial dilution in 96 well plates in the presence of G418 for a further 4-8 weeks. Positive clones were expanded and tested for correct expression by Western blot and fluorescence microscopy. HEK293T cells stably expressing NLRP3 constructs were maintained in

DMEM/F12 (1:1) supplemented with 10% FCS, 2 mM Glutamax, and 1% penicillin–streptomycin. All cells were routinely tested for Mycoplasma contamination with a Mycoplasma Detection Kit (Roche).

Differentiation and stimulation of bone marrow derived macrophages. Bone marrow derived macrophages (BMDMs) were obtained from wild-type mice by differentiating bone marrow cells for 7 days in DMEM (Lonza) supplemented with 25% of L929 medium, 15% FCS, 100 U/ml penicillin/streptomycin, and 2 mM Glutamax as described elsewhere (*42*). Cells were primed for 4 h with *E. coli* LPS O55:B5 (1 μg/ml, Invivogen), then washed in E-total buffer (147 mM NaCl, 10 mM HEPES, 13 mM glucose, 2 mM $CaCl_2$, 1 mM $MgCl_2$, and 2 mM KCl, pH 7.4) and treated for 30 min with nigericin (10 μM, Sigma), for 2 h with valinomycin (50 μM, Sigma) or for 2 h with BB15C5 (50 μM, Sigma). In some experiments, stimulations were performed in an E-total buffer with increased concentration of KCl or changing KCl for RbCl, LiCl or CsCl (as denoted in the figure legends), in that case the increase in the concentration of KCl, RbCl, LiCl or CsCl was accompanied with a reduction of the NaCl concentration to maintain isotonic conditions.

Retroviral production, immortalized macrophage generation and stimulation. For doxycycline-inducible expression of NLRPs constructs in immortalized mouse macrophages we used Tet-ON retroviral system (#631188, Clontech). The different NLRPs constructs (deletions or chimeras) were subcloned into pRETROX Tre3G plasmid (Clontech) using *Bam*HI/*Eco*RI and transfected using Lipofectamine 2000 into the packaging cell line Gryphon Ampho cell line (Alelle Biotechnology, ABP-RVC-10001). *Nlrp3*$^{-/-}$ immortalized mouse macrophages stably expressing the Tet-On 3G transactivator (*31*) were transduced with different NLRPs constructs or empty vector

encoding retroviruses for two days. Then positive macrophages were selected with puromycin (6 μg/mL) and G418 (1.5 mg/ml). For experiments, immortalized mouse macrophages were treated for 16 h with doxycycline (1 μg/ml, Sigma) and ultrapure LPS 0111:B4 (100 ng/ml, Invivogen) and then stimulated for 1 h with nigericin (10 μM, Sigma), or *C. difficile* toxin B (TcdB, 1 μg/ml, BML-G150-0050, Enzo), or 6 h with imiquimod (100 μM, tlrl-imqs, Invivogen), or for 16 h with MSU crystals (300 μg/ml, ALX-400-047-M002, Enzo) or with transfected lipoteichoic acid (15 μg/ml, tlrl-pslta, Invivogen). The specific NLRP3 inhibitor MCC950 (10 μM, CP-456773, Sigma) or the caspase-1 inhibitor IV Ac-YVAD-AOM (100 μM, 400015, Calbiochem) were added 30 minutes before and during the different stimulations.

***In vivo* MSU model**. All experimental protocols for animal handling were refined and approved by the Ethical Committee for Animal Research of the University of Murcia (reference 542/2019). C57BL/6J mice (WT, wild-type) were obtained from Charles River and inbreed at the specific pathogen-free animal house of the IMIB-Arrixaca up to F3 generation before getting new founders and NLRP3-deficient (*Nlrp3*$^{-/-}$) in C57BL/6J background were already described (*38*). Mice were bred in specific pathogen-free conditions with a 12:12 h light-dark cycle and used in accordance with the Spanish national (RD 1201/2005 and Law 32/2007) and EU (86/609/EEC and 2010/63/EU) legislation. *Nlrp3*$^{-/-}$ immortalized mouse macrophages expressing different NLRs or chimeric NLRs were treated *in vitro* for 16 h with doxycycline (1 μg/ml). Besides, mice were given doxycycline (2 mg/ml) and sucrose (5%, Sigma) in the drinking water one day before experimental initiation. Mice between 8-10 weeks of age receive an intraperitoneal (i.p.) injection of 2x10^6 immortalized macrophages and in some experiments the macrophages were stained for 15 min with carboxyfluorescein succinimidyl ester (CFSE, 10 μM, Thermo Fisher) before injection. After 3 h of

macrophages homing in the recipients, the animals received an i.p. injection of MSU crystals (40 mg/kg, ALX-400-047-M002, Enzo). After 16 h, animals were euthanized with CO_2 inhalation and peritoneal lavages were collected after exposing the abdominal wall by opening the skin and 4 ml of sterile saline solution were injected into the peritoneal cavity via a 25 gauge needle. The abdomen was gently massaged for 1 min and the peritoneal fluid was recovered through the needle and centrifuged at 433 *g* for 10 min. The cellular pellet was immediately used for flow cytometry and the supernatant were stored at -80 ºC until further ELISA analysis.

Flow cytometry. $5x10^5$ cells from mice peritoneal lavage were incubated with anti-CD16/32 (clone 93, 14-0161-85, eBioscience, 1:200) and then stained with anti-F4/80-Alexa Fluor 488 (clone BM8, 123119, Biolegend, 1:200), anti-CD11b-APC (clone M1/70, 101211, Biolegend, 1:200) and anti-Ly6G-PE (clone 1A8, 127607, Biolegend, 1:200). Granulocytes were identified as $CD11b^+F4/80^-Ly6G^+$ (**Figure S10A**). In some experiments, the presence of injected immortalized macrophages were monitored by $F4/80^+CSFE^+$ cells (**Figure S10B**), for that the anti-F4/80-APC antibody was used (clone BM8, 123115, Biolegend, 1:200). Samples were analyzed in a FACS Canto (BD Biosciences) by gating for singlets based on forward and side scatter parameters (**Figure S10A,B**). The data were analyzed by FCS Express 5 software (DeNovo Software).

ELISA and multiplex assay. Cell-free peritoneal lavage and macrophage supernatants were tested by ELISA for mouse IL-1β or IL-6 following manufacturer's instructions (R&D Systems and eBioscience respectively) and read in a Synergy Mx (BioTek) plate reader. Multiplexing for CXCL1, CXCL10, IL-18, IL-6, and CCL2 from peritoneal lavages was performed using the ProcartaPlex Multiplex Immunoassay (Invitrogen) following the manufacturer's indications, and analyzed in a Bio-Plex analyzer (Bio-Rad).

Western blot. Cells were lysed for 30 min on ice in cold lysis buffer (50 mM Tris-HCl pH 8.0, 150 mM NaCl, 2% Triton X-100, supplemented with 100 μl/ml of protease inhibitor mixture from Sigma) and then were centrifuged at 16,000 *g* for 15 min at 4 °C. Proteins in cell culture supernatants were concentrated using a 10 kDa cut-off column (Microcon, Merk-Millipore) by centrifugation at 11,200 *g* for 30 min at 4 °C. Cells lysates and concentrated supernatants were resolved in 4–12% precast Criterion polyacrylamide gels (Bio-Rad) and transferred to nitrocellulose membranes (Bio-Rad) by electroblotting. Membranes were probed with anti-GSDMD rabbit monoclonal (EPR19828, ab209845, Abcam, 1:5000), anti-IL-1β rabbit polyclonal (H-153; sc-7884, 1:1000), anti-caspase-1 rabbit polyclonal (sc-514, Santa Cruz, 1:1000), horseradish peroxidase-anti-β-actin (C4; sc-47778HRP, Santa Cruz, 1:10000) and anti-GFP rabbit polyclonal (ab6556, Abcam, 1:2500). HRP-conjugated secondary antibodies were from GE Healthcare. Full uncropped Western blots are presented in Supplementary **Figure S11**.

Quantitative reverse transcriptase–polymerase chain reaction (RT-PCR) analysis. Total RNA purification was performed using the RNAesy kit (Qiagen) according to manufacturer's recommendations and quantified on a nanodrop 2000 (Thermo Fisher). Detailed methods used for qRT-PCR have been described previously (*42*). Briefly, Reverse transcription was realized using iScriptTM cDNA Synthesis kit (BioRad). qPCR was performed in an iQTM 5 Real Time PCR detection System (BioRad) with a SYBR Green mix (Takara) and primers used were obtained from Sigma-Aldrich (KiCqStart® Primers) The presented relative gene expression levels were calculated using the $2^{-\Delta Ct}$ method normalizing to *Hprt1* expression as endogenous control.

BRET. HEK293T cells expressing the different NLRP3 BRET sensors (wild-type, mutations and deletions) were plated on a poly-L-lysine–coated white opaque 96-well plate; after adhesion, cells were incubated with different treatments in E-total (with different ionic composition, as stated in the figure legends) or vehicle and BRET readings were performed 5 min after the addition of 5 μM coelenterazine-H substrate. BRET signals were detected with two filter settings (*Renilla*-luciferase (Luc) filter [485 ± 20 nm] and YFP filter [530 ± 25 nm]) at 37 ºC using the Synergy Mx plate reader (BioTek) as described before (*25*). In some experiments, BRET signal was recorded every 35 seconds before and after nigericin, valinomycin, BB15C5 or ATP (this one over HEK293T cells expressing P2X7 receptor) automatic injection for a total of 15 min. For experiments measuring basal BRET signal, a stable signal for 5 min kinetic was recorded and averaged. For some experiments, nigericin or imiquimod was added to the plate and place in the incubator for 60 min or 6 h respectively, then coelenterazine-H was added and after 5 min of signal stabilization, BRET was recorded for 20 min. Titration was performed by transfection of different amounts of the plasmids used in this study (pcDNA empty plasmid was used to have equal amounts of total DNA in all the transfections). Expression of the different sensors was monitored by reading YFP fluorescence in the plate reader or by assessing individual cell relative fluorescence by fluorescence microscopy. Titration of the sensor will determine if the recorded BRET is intra- or inter-molecular, since intra-molecular energy transfer results in a stable BRET signal as the BRET sensor concentration increase and inter-molecular BRET will result in a proportional increases of the BRET signal as the sensor concentration increases (*25*). The BRET ratio was defined as the difference of the emission ratio 530 nm/485 nm of the BRET sensor minus this ratio of the Luc only tagged NLRP3. Results were expressed in milliBRET units (mBU).

Fluorescence microcopy. Following procedures previously described in (*22*), we seeded 5x10^4 HEK293T cells or *Nlrp3*$^{-/-}$ immortalized macrophages expressing the different NLRPs constructs tagged with YFP at N-terminus in poly-L-lysine coated coverslips (Corning). Cells were treated and stimulated as indicated in the figure legends, washed twice with PBS and fixed for 15 min at room temperature with 4% paraformaldehyde, and then were washed three times with PBS. For ASC immunofluorescence procedures have been previously described in (*22*), in particular cells were blocked with 2% bovine serum albumin and permeabilized with 0.2% Triton X-100 (Sigma) for 20 min at room temperature. Then cells were stained for 1.5 h at room temperature with the primary monoclonal mouse antibody anti-ASC (HASC-71, Biolegend, 1:1000). Cells were washed and then incubated for 1 h at room temperature with anti-mouse IgG fluorescence-conjugated secondary antibody (Alexa 647 donkey anti-mouse IgG (H+L), Life Technologies, 1:200). Cells were washed and nuclei stained for 10 min with DAPI (1:10000, Sigma) and coverslips were mounted on slides with mounting medium (S3023, Dako). Images were acquired using the same equipment that in previous studies (*22*), and we used a Nikon Eclipse *Ti* microscope equipped with a 20x S Plan Fluor objective (numerical aperture, 0.45) and a 60x Plan Apo Vc objective (numerical aperture, 1.40) and a digital Sight DS-QiMc camera (Nikon) with a Z optical with spacing of 0.4 μm and 387-nm/447-nm, 472-nm/520-nm, 543-nm/593-nm and 650-nm/668-nm filter sets (Semrock) and the NIS-Elements AR software (Nikon). Images were analyzed with ImageJ (US National Institutes of Health).

Measurement of intracellular K^+. 12 well plates with 10^6 BMDMs/well were stimulated for 4 h with LPS (1 μg/ml) at 37 ºC, then washed twice with E-total buffer and stimulated for 30 min at 37 ºC with different concentrations of nigericin as indicated in the figures legends or for 2 h with valinomycin (50 μM) or BB15C5 (50 μM). Then cells were briefly and quickly washed with nuclease-free water to avoid an osmotic shock and immediately

after cells were scraped in 200 μl/well of nuclease-free water followed by 3 freeze-thaw cycles. Lysates were centrifuged at 16000 *g* for 10 min at 4 ºC and the supernatants were stored at -80 ºC until K^+ concentration was quantified by indirect potentiometry using a Cobas 6000 with ISE module (Roche).

Bioinformatic analysis and modeling. NLRP3 sequence annotation and numbering was used from UNIPROT database (Q96P20). Multiple protein sequence alignment was performed using Clustal omega (*43*). FISNA domain signature was obtained by SMART database (*44*) and secondary FISNA domain prediction by Jpred 4 (*45*). The structure of human NLRP3 in complex with NEK7 and ADP as ligand in the NACHT domain, is taken from the PDB (*46*) structure with code 6NPY (*28*). Several loop regions are missing in this structure, as well as the PYD domain, the linker and most of the FISNA domain. We used the structure of NAIP2/NLRC4 inflammasome complex (3JBL) to infer the relocation of NACHT and LRR domains in the active oligomeric conformation of NLRP3. Then we used the superposition between the monomers of NLRP3 and NLRC4 to identify the fragments of NLRP3 that move when opening the conformation of NLRP3. The hinge is found in the loop region 417-441 (inside HD1 motif) between α-helices 9 and 10 of the NACHT domain (**Figure S2A**). We split the closed structure of NLRP3 around the hinge and superposed with MatchMaker (*47*) the two separated fragments, including the interaction with NEK7 and ADP as ligand (**Figure S12A**). We constructed the scaffold of the open conformation of NLRP3 by merging the two separated and superposed fragments. We then used the scaffold of NLRP3 in open conformation as template to model the sequence of NLRP3 starting at position 135 (i.e. except for the N-tail fragment, composed by the linker and the PYD domain). We used SABLE (*48*) to predict the secondary structure of the missing loops in the structure of NLRP3 and NEK7. Helices are predicted at NLRP3 positions 113-128 (in the linker between FISNA and PYD domains), 182-190 (in the FISNA domain) and 180-193 in the structure of NEK7. A strand

is formed in NLRP3 between residues 174-179 of the FISNA domain, forming a sheet with strand 364-369 with main-chain hydrogen-bonding interactions in anti-parallel, stabilized by an α–helix (**Figure S12B**). The rest of loops, in particular fragments 581-618 and 655-684 of NLRP3 and 180-193 of NEK7 were modelled with ModLoop (*49*) restricting the predicted helices (**Figure S12B**). We then used the structures of NAIP2/NLRC4 complex (3JBL) and the ASC^{PYD} assembly (3J63) to construct a model of the NLRP3 complex of inflammasome that includes the oligomerization of ASC^{PYD}. First, eleven models of monomeric NLRP3 in open conformation, interacting with NEK7 and ADP, without the PYD domain and the linker fragment that joints PYD and FISNA domains, were superposed with each monomer of NAIP2/NLRC4 in the structure 3JBL. The monomers of NLRP3 and NEK7 are merged into a single PDB file, forming a complex of 22 monomers. Second, we manually placed the complex of ASC^{PYD} assembly near the N-tail of the monomeric models of NRLP3, forming a starting fiber of ASC^{PYD} and preserving the symmetry of the complex (**Figure S13A**). Third, we used the PYD domain of NLRP3 from 3QF2. Then, taking into account that the complex of ASC^{PYD} is formed by layers of 6 monomers, we built the model of the full sequence of NLRP3 (**Figure S13A**) with MODELLER (*50*) upon an artificial template construction where the closest 11 monomers of ASC^{PYD} to $NLRP3^{NACHT}$ were substituted by the PYD domain of NLRP3 as follows: 1) for each pair of close monomers of NRLP3 we associated an ASC^{PYD} chain of the closest layer and another from the next layer (**Figure S13B**); 2) we selected the initial 11 chains of ASC^{PYD} and superpose 11 models of the PYD domain of NLRP3 in each chain; 3) we merged in the same chain one PYD domain with the rest of the structure of NRLP3 (C-tail fragment composed by domains FISNA, NACHT and LRR) associated with it. Finally, we used another structure of 3J63 to superpose 13 additional chains of ASC. We used MODELLER to model the whole complex, formed by 13 ASC^{PYD} chains, 11 full chains of NLRP3 and 11 chains of a partial structure of NEK7 (only the domain with structure in 6NPY). We forced the symmetry between the chains of NEK7 and the chain-fragments composed by FISNA-NACHT-LRR domains of NLRP3. The

structure of the linker was modelled as a loop, but forcing an α-helix in position 113-128 (**Figure S13C**). The different symmetry between NLRP3/NEK7 (with a C_{11} rotation axis) and the fiber of ASC^{PYD} (with a C_6 rotation axis) leaved the starting position of a chain of ASC^{PYD} as a seed to continue forming the ASC^{PYD} fiber (**Figure S13D**).

Statistical analysis. Statistical analyses were performed using GraphPad Prism 7 (Graph-Pad Software, Inc). Outliers were identified using the ROUT method and removed from statistics. For two-group comparisons, Mann-Whitney test was used; when compared three or more groups, Kruskal-Wallis test was used. All data are shown as mean values and error bars represent standard error from the number of independent assays indicated in the figure legend and plotted in histograms as dots. *p* value is indicated as $*p < 0.05$; $**p < 0.01$; $***p < 0.001$; $p > 0.05$ not significant (*ns*).

Acknowledgments: We thank KA. Fitzgerald for immortalized NLRP3-deficient macrophages and I. Couillin for *Nlrp3*$^{-/-}$ mice. We also thank A.I. Gómez (IMIB-Arrixaca, Murcia, Spain) for technical assistance with molecular and cellular biology, F. Noguera and M. Martínez (IMIB-Arrixaca, Murcia, Spain) for running Hitachi ion detection system, and the members of the Pelegrin's laboratory for comments and suggestions thought the development of this project, in particular to M. Mateo. We also want to acknowledge the support of the SPF-animal house from IMIB-Arrixaca.

Funding: I.H.-B. would like to acknowledge the funding by the Slovenian Research Agency (project grant J3-1746 and core funding P4-0176) and B.O. would like to acknowledge the funding by the *Ministerio de Economía, Industria y Competitividad* and ERDF (BIO2017-85329-R). This work was supported by grants to A.T-A. from the internal support program of the Medical Faculty, University of Tübingen, Fortüne-Antrag Nr. 2615-0-0 and to P.P. from *FEDER/Ministerio de Ciencia, Innovación y Universidades – Agencia Estatal de Investigación* (grant SAF2017-88276-R), *Fundación Séneca* (grants 20859/PI/18, 21081/PDC/19 and 0003/COVI/20), and the European Research Council (ERC-2013-CoG grant 614578 and ERC-2019-PoC grant 899636).

Author contributions: A.T-A. and D.A-B. equally performed most of the experimental work; C.A-V. performed the *in vivo* model; M.C.B. performed part of the molecular biology, transfections and stable cell line generation; I.H-B. set up retroviral expression system in immortalized macrophage lines; A.T-A. established the different immortalized macrophage cell lines and conceived and performed analysis of the NLRP3 exon 3 linker sequence; B.O. and D.A-B. performed bioinformatic structural analysis; A.T-A., D.A-B., C.A-V. and P.P. analysed the data, interpreted results and conceived the experiments; P.P. prepared the figures with the help of A.T-A., D.A-B., C.A-V. and B.O.; A.T-A., D.A-B., B.O., I.H-B. and C.A-V. contributed to paper writing; P.P. conceived the project, provided funding, wrote the paper and overall supervision of this study.

Competing Interests: P.P. declares that he is an inventor in a patent filed on 12 March 2020 by the *Fundación para la Formación e Investigación Sanitaria de la Región de Murcia* (PCT/EP2020/056729) for a method to identify NLRP3-immunocompromised sepsis patients. The remaining authors declare no competing interests.

Data and materials availability: All data needed to evaluate the conclusions of the paper are present in the paper and/or the Supplementary Materials. No materials used in this study are subject to an MTA. All materials are available upon reasonable request to the corresponding author.

List of Supplementary Materials:

Figure S1. Intracellular K^+-efflux activates NLRP3.

Figure S2. A closed NLRP3 structure presents a shielded nucleotide binding pocket.

Figure S3. NLRP3 PYD domain is not necessary for NLRP3 oligomerization, but is required to form active NLRP3 oligomers.

Figure S4. NLRP3 N-terminus sequence features.

Figure S5. Model of ASC^{PYD}-NLRP3-NEK7 oligomer.

Figure S6. NLRP3 linker and FISNA domain in inflammasome activation.

Figure S7. Comparison of the N-terminal sequence of NLRP3 and NLRP6.

Figure S8. NLRP6 is not activated in response to K^+ efflux.

Figure S9. Reconstitution of *Nlrp3*$^{-/-}$ mice with macrophages expressing NLRP6 chimeric receptor harbouring the NLRP3 PYD-linker-FISNA.

Figure S10. Flow cytometry gating strategy.

Figure S11. Uncropped Western blots of main figures.

Figure S12. Model of NLRP3 monomer in open and closed conformation.

Figure S13. Modelling NLRP3 oligomer.

Source data for Figures 1 to 8.

REFERENCES

1. K. V. Swanson, M. Deng, J. P.-Y. Ting, The NLRP3 inflammasome: molecular activation and regulation to therapeutics. *Nat. Rev. Immunol.* **19**, 477–489 (2019).

2. M. S. J. Mangan, E. J. Olhava, W. R. Roush, H. M. Seidel, G. D. Glick, E. Latz, Targeting the NLRP3 inflammasome in inflammatory diseases. *Nat. Rev. Drug Discov.* **17**, 588–606 (2018).

3. Y. He, M. Y. Zeng, D. Yang, B. Motro, G. Núñez, NEK7 is an essential mediator of NLRP3 activation downstream of potassium efflux. *Nature*. **530**, 354–357 (2016).

4. J. Chen, Z. J. Chen, PtdIns4P on dispersed trans-Golgi network mediates NLRP3 inflammasome activation. *Nature*. **564**, 71–76 (2018).

5. R. Zhou, A. Tardivel, B. Thorens, I. Choi, J. Tschopp, Thioredoxin-interacting protein links oxidative stress to inflammasome activation. *Nat. Immunol.* **11**, 136–140 (2009).

6. N. Subramanian, K. Natarajan, M. R. Clatworthy, Z. Wang, R. N. Germain, The Adaptor MAVS Promotes NLRP3 Mitochondrial Localization and Inflammasome Activation. *Cell*. **153**, 348–361 (2013).

7. X. Li, S. Thome, X. Ma, M. Amrute-Nayak, A. Finigan, L. Kitt, L. Masters, J. R. James, Y. Shi, G. Meng, Z. Mallat, MARK4 regulates NLRP3 positioning and inflammasome activation through a microtubule-dependent mechanism. *Nat. Commun.* **8**, 15986 (2017).

8. P. Samir, S. Kesavardhana, D. M. Patmore, S. Gingras, R. K. S. Malireddi, R. Karki, C. S. Guy, B. Briard, D. E. Place, A. Bhattacharya, B. R. Sharma, A. Nourse, S. V. King, A. Pitre, A. R. Burton, S. Pelletier, R. J. Gilbertson, T.-D.

Kanneganti, DDX3X acts as a live-or-die checkpoint in stressed cells by regulating NLRP3 inflammasome. *Nature*. **573**, 590–594 (2019).

9. Y. Duan, L. Zhang, D. Angosto-Bazarra, P. Pelegrín, G. Núñez, Y. He, RACK1 Mediates NLRP3 Inflammasome Activation by Promoting NLRP3 Active Conformation and Inflammasome Assembly. *Cell Rep.* **33**, 108405 (2020).

10. T. Próchnicki, M. S. Mangan, E. Latz, Recent insights into the molecular mechanisms of the NLRP3 inflammasome activation. *F1000Research*. **5**, 1415–1469 (2016).

11. I. Hafner-Bratkovič, P. Pelegrín, Ion homeostasis and ion channels in NLRP3 inflammasome activation and regulation. *Curr. Opin. Immunol.* **52**, 8–17 (2018).

12. R. Muñoz-Planillo, P. Kuffa, G. Martínez-Colón, B. Smith, T. Rajendiran, G. Núñez, K+ Efflux Is the Common Trigger of NLRP3 Inflammasome Activation by Bacterial Toxins and Particulate Matter. *Immunity*. **38**, 1142–1153 (2013).

13. A. Lu, V. G. Magupalli, J. Ruan, Q. Yin, M. K. Atianand, M. R. Vos, G. F. Schröder, K. A. Fitzgerald, H. Wu, E. H. Egelman, Unified Polymerization Mechanism for the Assembly of ASC-Dependent Inflammasomes. *Cell*. **156**, 1193–1206 (2014).

14. F. I. Schmidt, A. Lu, J. W. Chen, J. Ruan, C. Tang, H. Wu, H. L. Ploegh, A single domain antibody fragment that recognizes the adaptor ASC defines the role of ASC domains in inflammasome assembly. *J. Exp. Med.* **213**, 771–90 (2016).

15. M. S. Dick, L. Sborgi, S. Rühl, S. Hiller, P. Broz, ASC filament formation serves as a signal amplification mechanism for inflammasomes. *Nat. Commun.* **7**, 11929 (2016).

16. D. Boucher, M. Monteleone, R. C. Coll, K. W. Chen, C. M. Ross, J. L. Teo, G. A. Gomez, C. L. Holley, D. Bierschenk, K. J. Stacey, A. S. Yap, J. S. Bezbradica, K.

Schroder, Caspase-1 self-cleavage is an intrinsic mechanism to terminate inflammasome activity. *J. Exp. Med.* **215**, 827–840 (2018).

17. P. Broz, P. Pelegrín, F. Shao, The gasdermins, a protein family executing cell death and inflammation. *Nat. Rev. Immunol.* **20**, 143–157 (2020).

18. A. Baroja-Mazo, F. Martín-Sánchez, A. I. Gomez, C. M. Martínez, J. Amores-Iniesta, V. Compan, M. Barberà-Cremades, J. Yagüe, E. Ruiz-Ortiz, J. Antón, S. Buján, I. Couillin, D. Brough, J. I. Arostegui, P. Pelegrín, F. Martin-Sanchez, A. I. Gomez, C. M. Martínez, J. Amores-Iniesta, V. Compan, M. Barberà-Cremades, J. Yagüe, E. Ruiz-Ortiz, J. Antón, S. Buján, I. Couillin, D. Brough, J. I. Aróstegui, P. Pelegrin, The NLRP3 inflammasome is released as a particulate danger signal that amplifies the inflammatory response. *Nat. Immunol.* **15**, 738–748 (2014).

19. B. S. Franklin, L. Bossaller, D. De Nardo, J. M. Ratter, A. Stutz, G. Engels, C. Brenker, M. Nordhoff, S. R. Mirandola, A. Al-Amoudi, M. S. Mangan, S. Zimmer, B. G. Monks, M. Fricke, R. E. Schmidt, T. Espevik, B. Jones, A. G. Jarnicki, P. M. Hansbro, P. Busto, A. Marshak-Rothstein, S. Hornemann, A. Aguzzi, W. Kastenmüller, E. Latz, The adaptor ASC has extracellular and “prionoid” activities that propagate inflammation. *Nat. Immunol.* **15**, 727–737 (2014).

20. C. Venegas, S. Kumar, B. S. Franklin, T. Dierkes, R. Brinkschulte, D. Tejera, A. Vieira-Saecker, S. Schwartz, F. Santarelli, M. P. Kummer, A. Griep, E. Gelpi, M. Beilharz, D. Riedel, D. T. Golenbock, M. Geyer, J. Walter, E. Latz, M. T. Heneka, Microglia-derived ASC specks cross-seed amyloid-β in Alzheimer’s disease. *Nature*. **552**, 355–361 (2017).

21. V. Petrilli, S. Papin, C. Dostert, A. Mayor, F. Martinon, J. Tschopp, Activation of the NALP3 inflammasome is triggered by low intracellular potassium concentration. *Cell Death Differ.* **14**, 1583–1589 (2007).

22. A. Tapia-Abellán, D. Angosto-Bazarra, H. Martínez-Banaclocha, C. de Torre-Minguela, J. P. Cerón-Carrasco, H. Pérez-Sánchez, J. I. Arostegui, P. Pelegrin, MCC950 closes the active conformation of NLRP3 to an inactive state. *Nat. Chem. Biol.* **15**, 560–564 (2019).

23. E. Bartok, M. Kampes, V. Hornung, in *Methods in molecular biology*, F. Di Virgilio, P. Pelegrin, Eds. (Springer Basel, 2016), vol. 1417, pp. 97–113.

24. V. Compan, A. Baroja-Mazo, G. López-Castejón, A. I. Gomez, C. M. Martínez, D. Angosto, M. T. Montero, A. S. Herranz, E. Bazán, D. Reimers, V. Mulero, P. Pelegrín, Cell Volume Regulation Modulates NLRP3 Inflammasome Activation. *Immunity*. **37**, 487–500 (2012).

25. F. Martín-Sánchez, V. Compan, P. Pelegrín, in *Methods in Molecular Biology*, F. Di Virgilio, P. Pelegrin, Eds. (Springer Basel, Basel, 2016), vol. 1417, pp. 159–168.

26. F. Martin-Sanchez, C. Diamond, M. Zeitler, A. I. A. I. A. I. I. A. Gomez, A. Baroja-Mazo, J. Bagnall, D. Spiller, M. White, M. M. J. D. M. J. D. Daniels, A. Mortellaro, M. Penalver, P. Paszek, J. P. J. P. J. P. Steringer, W. Nickel, D. Brough, P. Pelegrin, F. Martín-Sánchez, C. Diamond, M. Zeitler, A. Gomez-Sánchez, M. Peñalver, P. Paszek, J. P. J. P. J. P. Steringer, W. Nickel, D. Brough, P. Pelegrín, A. I. A. I. A. I. I. A. Gomez, A. Baroja-Mazo, J. Bagnall, D. Spiller, M. White, M. M. J. D. M. J. D. Daniels, A. Mortellaro, M. Peñalver, P. Paszek, J. P. J. P. J. P. Steringer, W. Nickel, D. Brough, P. Pelegrín, P. Pelegrin, F. Martín-Sánchez, C. Diamond, M. Zeitler, A. I. A. I. A. I. I. A. Gomez, A. Baroja-Mazo, J. Bagnall, D. Spiller, M. White, M. M. J. D. M. J. D. Daniels, A. Mortellaro, M. Peñalver, P. Paszek, J. P. J. P. J. P. Steringer, W. Nickel, D. Brough, P. Pelegrín, A. Gomez-Sánchez, M. Peñalver, P. Paszek, J. P. J. P. J. P. Steringer, W. Nickel, D. Brough, P. Pelegrín, A. I. A. I. A. I. I. A. Gomez, A. Baroja-Mazo, J.

Bagnall, D. Spiller, M. White, M. M. J. D. M. J. D. Daniels, A. Mortellaro, M. Peñalver, P. Paszek, J. P. J. P. J. P. Steringer, W. Nickel, D. Brough, P. Pelegrin, Inflammasome-dependent IL-1β release depends upon membrane permeabilisation. *Cell Death Differ.* **23**, 1219–1231 (2016).

27. M. Cocco, C. Pellegrini, H. Martínez-Banaclocha, M. Giorgis, E. Marini, A. Costale, G. Miglio, M. Fornai, L. Antonioli, G. López-Castejón, A. Tapia-Abellán, D. Angosto, I. Hafner-Bratkovič, L. Regazzoni, C. Blandizzi, P. Pelegrín, M. Bertinaria, Development of an Acrylate Derivative Targeting the NLRP3 Inflammasome for the Treatment of Inflammatory Bowel Disease. *J. Med. Chem.* **60**, 3656–3671 (2017).

28. H. Sharif, L. Wang, W. L. Wang, V. G. Magupalli, L. Andreeva, Q. Qiao, A. V. Hauenstein, Z. Wu, G. Núñez, Y. Mao, H. Wu, Structural mechanism for NEK7-licensed activation of NLRP3 inflammasome. *Nature*. **570**, 338–343 (2019).

29. L. Zhang, S. Chen, J. Ruan, J. Wu, A. B. Tong, Q. Yin, Y. Li, L. David, A. Lu, W. L. Wang, C. Marks, Q. Ouyang, X. Zhang, Y. Mao, H. Wu, Cryo-EM structure of the activated NAIP2-NLRC4 inflammasome reveals nucleated polymerization. *Sci. (New York, NY)*. **350**, 404–409 (2015).

30. J. A. Duncan, D. T. Bergstralh, Y. Wang, S. B. Willingham, Z. Ye, A. G. Zimmermann, J. P.-Y. Ting, Y. Nakamura, N. Kambe, M. Saito, R. Nishikomori, Y. G. Kim, M. Murakami, G. Nunez, H. Matsue, Cryopyrin/NALP3 binds ATP/dATP, is an ATPase, and requires ATP binding to mediate inflammatory signaling. *Proc. Natl. Acad. Sci.* **104**, 8041–8046 (2007).

31. I. Hafner-Bratkovič, P. Sušjan, D. Lainšček, A. Tapia-Abellán, K. Cerović, L. Kadunc, D. Angosto-Bazarra, P. Pelegrín, R. Jerala, NLRP3 lacking the leucine-rich repeat domain can be fully activated via the canonical inflammasome pathway. *Nat. Commun.* **9**, 5182 (2018).

32. R. C. Coll, J. R. Hill, C. J. Day, A. Zamoshnikova, D. Boucher, N. L. Massey, J. L. Chitty, J. A. Fraser, M. P. Jennings, A. A. B. Robertson, K. Schroder, MCC950 directly targets the NLRP3 ATP-hydrolysis motif for inflammasome inhibition. *Nat. Chem. Biol.* **15**, 556–559 (2019).

33. H. Hara, S. S. Seregin, D. Yang, K. Fukase, M. Chamaillard, E. S. Alnemri, N. Inohara, G. Y. Chen, G. Núñez, The NLRP6 Inflammasome Recognizes Lipoteichoic Acid and Regulates Gram-Positive Pathogen Infection. *Cell*. **175**, 1651-1664.e14 (2018).

34. P. K. Anand, R. K. Malireddi, J. R. Lukens, P. Vogel, J. Bertin, M. Lamkanfi, T. D. Kanneganti, NLRP6 negatively regulates innate immunity and host defence against bacterial pathogens. *Nature*. **488**, 389–393 (2012).

35. V. Rabolli, L. Wallemme, S. Lo Re, F. Uwambayinema, M. Palmai-Pallag, L. Thomassen, D. Tyteca, J.-N. N. Octave, E. Marbaix, D. Lison, O. Devuyst, F. Huaux, Critical role of aquaporins in interleukin 1β (IL-1β)-induced inflammation. *J. Biol. Chem.* **289**, 13937–13947 (2014).

36. A. Di, S. Xiong, Z. Ye, R. K. S. Malireddi, S. Kometani, M. Zhong, M. Mittal, Z. Hong, T.-D. Kanneganti, J. Rehman, A. B. Malik, The TWIK2 Potassium Efflux Channel in Macrophages Mediates NLRP3 Inflammasome-Induced Inflammation. *Immunity*. **49**, 56–65 (2018).

37. C. J. Groß, R. Mishra, K. S. Schneider, G. Médard, J. Wettmarshausen, D. C. Dittlein, H. Shi, O. Gorka, P.-A. Koenig, S. Fromm, G. Magnani, T. Ćiković, L. Hartjes, J. Smollich, A. A. B. Robertson, M. A. Cooper, M. Schmidt-Supprian, M. Schuster, K. Schroder, P. Broz, C. Traidl-Hoffmann, B. Beutler, B. Kuster, J. Ruland, S. Schneider, F. Perocchi, O. Groß, K+ Efflux-Independent NLRP3 Inflammasome Activation by Small Molecules Targeting Mitochondria. *Immunity*. **45**, 761–773 (2016).

38. A. Mayor, A. Tardivel, F. Martinon, V. Pe, V. Pétrilli, A. Mayor, A. Tardivel, J. Tschopp, Gout-associated uric acid crystals activate the NALP3 inflammasome. *Nature*. **440**, 237–241 (2006).

39. V. G. Magupalli, R. Negro, Y. Tian, A. V. Hauenstein, G. Di Caprio, W. Skillern, Q. Deng, P. Orning, H. B. Alam, Z. Maliga, H. Sharif, J. J. Hu, C. L. Evavold, J. C. Kagan, F. I. Schmidt, K. A. Fitzgerald, T. Kirchhausen, Y. Li, H. Wu, HDAC6 mediates an aggresome-like mechanism for NLRP3 and pyrin inflammasome activation. *Science (80-.).* **369**, eaas8995 (2020).

40. T.-D. Kanneganti, N. Özören, M. Body-Malapel, A. Amer, J.-H. Park, L. Franchi, J. Whitfield, W. Barchet, M. Colonna, P. Vandenabeele, J. Bertin, A. Coyle, E. P. Grant, S. Akira, G. Núñez, Bacterial RNA and small antiviral compounds activate caspase-1 through cryopyrin/Nalp3. *Nature*. **440**, 233–236 (2006).

41. M. T. Young, P. Pelegrin, P. Pelegrin, A. Surprenant, P. Pelegrin, A. Surprenant, Identification of Thr283 as a key determinant of P2X7 receptor function. *Br. J. Pharmacol.* **149**, 261–268 (2006).

42. J. J. Martínez-García, H. Martínez-Banaclocha, D. Angosto-Bazarra, C. de Torre-Minguela, A. Baroja-Mazo, C. Alarcón-Vila, L. Martínez-Alarcón, J. Amores-Iniesta, F. Martín-Sánchez, G. A. G. A. Ercole, C. M. C. M. Martínez, A. González-Lisorge, J. Fernández-Pacheco, P. Martínez-Gil, S. Adriouch, F. Koch-Nolte, J. Luján, F. Acosta-Villegas, P. Parrilla, C. García-Palenciano, P. Pelegrin, P2X7 receptor induces mitochondrial failure in monocytes and compromises NLRP3 inflammasome activation during sepsis. *Nat. Commun.* **10**, 2711 (2019).

43. F. Sievers, A. Wilm, D. Dineen, T. J. Gibson, K. Karplus, W. Li, R. Lopez, H. McWilliam, M. Remmert, J. Söding, J. D. Thompson, D. G. Higgins, Fast, scalable generation of high-quality protein multiple sequence alignments using Clustal Omega. *Mol. Syst. Biol.* **7**, 539 (2011).

44. I. Letunic, P. Bork, 20 years of the SMART protein domain annotation resource. *Nucleic Acids Res.* **46**, D493–D496 (2018).

45. A. Drozdetskiy, C. Cole, J. Procter, G. J. Barton, JPred4: a protein secondary structure prediction server. *Nucleic Acids Res.* **43**, W389–W394 (2015).

46. S. K. Burley, H. M. Berman, C. Bhikadiya, C. Bi, L. Chen, L. Di Costanzo, C. Christie, K. Dalenberg, J. M. Duarte, S. Dutta, Z. Feng, S. Ghosh, D. S. Goodsell, R. K. Green, V. Guranovic, D. Guzenko, B. P. Hudson, T. Kalro, Y. Liang, R. Lowe, H. Namkoong, E. Peisach, I. Periskova, A. Prlic, C. Randle, A. Rose, P. Rose, R. Sala, M. Sekharan, C. Shao, L. Tan, Y.-P. Tao, Y. Valasatava, M. Voigt, J. Westbrook, J. Woo, H. Yang, J. Young, M. Zhuravleva, C. Zardecki, RCSB Protein Data Bank: biological macromolecular structures enabling research and education in fundamental biology, biomedicine, biotechnology and energy. *Nucleic Acids Res.* **47**, D464–D474 (2019).

47. E. C. Meng, E. F. Pettersen, G. S. Couch, C. C. Huang, T. E. Ferrin, Tools for integrated sequence-structure analysis with UCSF Chimera. *BMC Bioinformatics*. **7**, 339 (2006).

48. R. Adamczak, A. Porollo, J. Meller, Combining prediction of secondary structure and solvent accessibility in proteins. *Proteins Struct. Funct. Bioinforma.* **59**, 467–475 (2005).

49. A. Fiser, A. Sali, ModLoop: automated modeling of loops in protein structures. *Bioinformatics*. **19**, 2500–1 (2003).

50. B. Webb, A. Sali, Protein Structure Modeling with MODELLER. *Methods Mol. Biol.* **1654**, 39–54 (2017).

FIGURE LEGENDS

Figure 1. K^+ efflux induces cells with multiple NLRP3 puncta.

(**A**) IL-1β release and intracellular K^+ concentration from LPS-primed bone marrow derived macrophages (BMDM) activated for 30 min with different doses of nigericin. *n*= 4-6 independent experiments for each concentration of nigericin.

(**B**) IL-1β release from LPS-primed BMDMs activated for 30 min with nigericin (10 μM) in the presence of increasing concentrations of KCl.

(**C**) IL-1β release from LPS-primed BMDMs activated for 30 min with nigericin (10 μM, top) or with *C. difficile* toxin B (TcdB, 1 μg/ml, bottom) in the absence/presence of 40 mM KCl, RbCl, CsCl or LiCl. *n*= 4 independent experiments; Kruskal-Wallis test.

(**D**) Representative fluorescent micrographs of HEK293T cells expressing YFP-NLRP3 (green) and stained for nuclei (DAPI, blue) treated for 30 min with nigericin (10 μM) in the absence/presence of 140 mM KCl. Scale bar 10 μm.

(**E**) Representative fluorescent micrographs of HEK293T cells (left) and *Nlrp3*$^{-/-}$ immortalized macrophages (iMos, right) expressing YFP-NLRP3 (green), ASC (stained in red) and stained for nuclei (DAPI, blue), treated for 30 and 60 min with nigericin (10 μM) respectively. Scale bar 20 μm (left) and 10 μm (right). Arrows denote ASC-specks; HEK293T cells were stably expressing YFP-NLRP3 and transfected for ASC.

Figure 2. K^+ efflux modifies the NLRP3 structure.

(**A**) Average BRET signal for YFP-NLRP3-Luc expressed in HEK293T cells before and after stimulation with nigericin (10 μM, denoted by a grey box), in the absence (left, middle) or presence (right) of 140 mM KCl; please note kinetics of BRET have been plotted with the same scale, but relatively at the same level to ease comparison. *n*=51, 4 and 6 for nigericin 15 min, 85 min and nigericin+KCl respectively; Mann-Whitney test.

(**B**) NLRP3 BRET signal variation after treatment for 15 min with nigericin (10 μM) vs basal conditions without nigericin in the presence of increasing concentrations of KCl. *n*= 3-5 independent cell culture wells for each KCl concentration.

(**C**) Average BRET signal for YFP-NLRP3-Luc expressed in HEK293T cells before and after stimulation with nigericin (10 μM) in the absence/presence of 40 mM RbCl or 40 mM LiCl; please note kinetics of BRET have been plotted with the same scale, but relatively at the same initial level to ease comparison. *n*= 12 independent cultures from 4 independent experiments; Mann-Whitney test.

(**D**) Average BRET signal for YFP-NLRP3-Luc expressed in HEK293T cells (top and middle) or HEK293T-P2X7 receptor (bottom), before and after stimulation with valinomycin (50 μM), BB15C5 (50 μM) or ATP (3 mM), in the absence/presence of 140 mM KCl; please note kinetics of BRET have been plotted with the same scale, but relatively at the same initial level to ease comparison. *n*= 6-18 independent cell cultures; Mann-Whitney test.

Figure 3. The PYD domain is dispensable for NLRP3 activation in response to K^+-efflux.

(**A**) Representative fluorescent micrographs of HEK293T cells expressing YFP-ΔPYD-NLRP3 (green) and stained for nuclei (DAPI, blue) treated for 30 min with nigericin (10 μM) in the absence/presence of 140 mM KCl. Scale bar 10 μm.

(**B**) Average BRET signal for YFP-ΔPYD-NLRP3-Luc expressed in HEK293T cells before and after stimulation with nigericin (10 μM), in the absence/presence of 140 mM KCl. *n*=5-17 independent cell cultures, from 3-5 independent experiments; please note kinetics of BRET have been plotted with the same scale, but relatively at the same initial level to ease comparison; Mann-Whitney test.

(**C**) IL-1β release from *Nlrp3*$^{-/-}$ immortalized macrophages (iMos) treated for 16h with doxycycline (1 μg/ml) and LPS (100 ng/ml) to induce the expression of YFP-ΔPYD-NLRP3 and then activated for 60 min with nigericin (10 μM). *n*= 3 independent experiments.

(**D**) Representative fluorescent micrographs of HEK293T cells expressing YFP-ΔPYD-NLRP3 or full-length NLRP3 as indicated (green) and ASC (red), stained for nuclei (DAPI, blue) treated for 30 min with nigericin (10 μM). Scale bar 20 μm.

Figure 4. Model of ASC^{PYD}-NLRP3-NEK7 oligomer.

(**A**) The structure on the left corresponds to a ribbon plot showing an oligomer complex of 11 NLRP3 monomers, 11 NEK7 and 11 ASC^{PYD} chains. The representation in the right shows the superposition of 11 NLRP3 monomers of the oligomer complex of the modelled inflammasome structure. PYD domains are placed at different distances of the NACHT domain depending on the conformation of the linker (shown in dark red in the right representation).

(**B**) Oligomer complex of 11 NLRP3 monomers, 11 NEK7 and 11 ASC^{PYD} chains. Linker fragment between PYD domains and FISNA domains of each NLRP3 are shown in dark red. FISNA domains of NLRP3 are shown in grey-blue highlighting the continuous connectivity through FISNA-FISNA and FISNA-NACHT interfaces. This model presents a compatible structure to promote ASC^{PYD} filament formation.

Figure 5. The sequence between PYD and NATCH domains is important for NLRP3 activation in response to K^{+}-efflux.

(**A**) IL-1β release from *Nlrp3*$^{-/-}$ immortalized macrophages (iMos) treated for 16 h with doxycycline (1 μg/ml) and LPS (100 ng/ml) to induce the expression of different truncations of NLRP3 as indicated and then activated for 60 min with nigericin (10 μM) in the absence/presence of 40 mM KCl. *n*= 2-5 independent experiments; Mann-Whitney test.

(**B**) Western blot for IL-1β, caspase-1, GSDMD, NLRP3 and β-actin, from cell lysates and supernatants of *Nlrp3*$^{-/-}$ iMos expressing YFP-Δ92-120-NLRP3 treated as in (A) in the absence/presence of MCC950 (10 μM); Representative of *n*= 2 independent experiments.

(**C**) Percentage of ASC specking *Nlrp3*$^{-/-}$ iMos expressing different truncations of NLRP3 treated as in (A). *n*= 3-27 independent experiments; Mann-Whitney test.

(**D**) Representative fluorescent micrographs of *Nlrp3*$^{-/-}$ iMos (top) and HEK293T cells (bottom) expressing different truncations of YFP-NLRP3 as indicated (green) and iMos stained for ASC (red, arrowheads denotes ASC specks quantified in panel C) and nuclei (DAPI, blue), treated for 60 and 30 min with nigericin (10 μM) respectively. Scale bar 10 μm. Quantification of HEK293T cells with NLRP3 punctuate staining is shown on the right of micrographs. *n*= 3-10 independent experiments.

(**E,F**) Average BRET signal for YFP-Δ92-120-NLRP3-Luc, YFP-Δ92-132-NLRP3-Luc, YFP-Δ92-148-NLRP3-Luc (**E**), or YFP-Δ149-180-NLRP3-Luc, YFP-Δ181-217-NLRP3-Luc (**F**) expressed in HEK293T cells before and after stimulation with nigericin (10 μM, indicated by an arrow), in the absence/presence of 140 mM KCl or MCC950 (10 μM); please note kinetics of BRET have been plotted with the same scale, but relatively at the same initial level to ease comparison. *n*= 2-19 independent cell cultures; Mann-Whitney test.

Figure 6. NLRP3 PYD-linker-FISNA sequence renders NLRP6 sensitive to K^+-efflux.

(**A**) IL-1β release from *Nlrp3*$^{-/-}$ immortalized macrophages (iMos) treated for 16 h with doxycycline (1 μg/ml) and LPS (100 ng/ml) to induce the expression of YFP-NLRP6, YFP-NLRP3 or YFP-chimeric NLRP3/6 as indicated and then activated for 60 min with nigericin (10 μM) in the absence/presence of 40 mM KCl; *n*= 4 independent experiments; Mann-Whitney test.

(**B**) Western blot for IL-1β, caspase-1, NLRP3/6 and β-actin, from cell lysates and supernatants of *Nlrp3*$^{-/-}$ iMos expressing YFP-NLRP3, YFP-NLRP3(1-217)-NLRP6(196-892), or YFP-NLRP6 treated as in (A); Representative of *n*= 3 independent experiments.

(**C**) IL-1β release (ELISA left, Western blot right) from *Nlrp3*$^{-/-}$ iMos expressing the chimera YFP-NLRP3(1-217)-NLRP6(196-892) treated as in (A) in the absence/presence of MCC950 (10 μM) or Ac-YVAD-AOM (YVAD, 100 μM). For the ELISA *n*= 4-6 independent experiments; Mann-Whitney test.

(**D**) Percentage of ASC specking in *Nlrp3*$^{-/-}$ iMos expressing the chimera YFP-NLRP3(1-217)-NLRP6(196-892) treated as in (A). *n*= 7-8 independent experiments; Mann-Whitney test.

(**E**) Percentage of ASC specking in HEK293T cells expressing ASC and the chimera YFP-NLRP3(1-217)-NLRP6(196-892) treated for 30 min with nigericin (10 μM) in the absence/presence of 140 mM KCl. *n*= 5-15 independent experiments; Kruskal-Wallis test.

(**F**) Representative fluorescent micrographs of HEK293T cells expressing the chimera YFP-NLRP3(1-217)-NLRP6(196-892) (green) and stained for nuclei (DAPI, blue), treated as in (E). Scale bar 10 μm. Right: quantification of YFP-NLRP3(1-217)-NLRP6(196-892) cells with a punctuate staining. *n*= 4 independent experiments; Mann-Whitney test.

Figure 7. NLRP6 with the PYD-linker-FISNA NLRP3 sequence is activated by MSU crystals and imiquimod.

(**A**) IL-1β release from *Nlrp3*$^{-/-}$ immortalized macrophages (iMos) expressing different truncations of NLRP3 as indicated treated for 16 h with doxycycline (1 μg/ml), LPS (100 ng/ml) and MSU crystals (300 μg/ml) in the absence/presence of 40 mM KCl. *n*= 3-4 independent experiments; Mann-Whitney test.

(**B**) IL-1β release from *Nlrp3*$^{-/-}$ iMos treated as in (A) but expressing different chimeric NLRP6/3 receptors as indicated. *n*= 3-4 independent experiments; Mann-Whitney test.

(**C**) IL-1β release from *Nlrp3*$^{-/-}$ iMos expressing different truncations of NLRP3 as indicated treated for 16 h with doxycycline (1 μg/ml) and LPS (100 ng/ml) to induce the expression of different NLRP3 truncations as indicated and then activated for 1 h with imiquimod (100 μM) in the absence/presence of 40 mM KCl. *n*= 3-4 independent experiments; Mann-Whitney test.

(**D**) IL-1β release from *Nlrp3*$^{-/-}$ iMos treated as in (C) but expressing different chimeric NLRP6/3 receptors as indicated. *n*= 3-4 independent experiments; Mann-Whitney test.
(**E**) Quantification of HEK293T cells expressing YFP-NLRP3 treated for different times with imiquimod (100 μM, for 0.5, 2, 4 or 6 h) or nigericin (10 μM, 30 min) in the absence/presence of 40 mM KCl. *n*= 3-4 independent experiments; Mann-Whitney test.
(**F**) Average BRET signal for YFP-NLRP3-Luc expressed in HEK293T cells before and after stimulation with imiquimod (100 μM, 6 h), in the absence or presence of 40 mM KCl. *n*= 6-9 independent measurements; Kruskal-Wallis test.

Figure 8. NLRP6 with the NLRP3 PYD-linker-FISNA sequence induces an inflammatory response to MSU crystals.

(**A**) Protocol followed in the experimental *in vivo* assay (top). IL-1β and IL-18 in the peritoneal lavage of *Nlrp3*$^{-/-}$ after an i.p. injection with *Nlrp3*$^{-/-}$ iMos expressing YFP-NLRP6, the chimera YFP-NLRP3(1-217)-NLRP6(196-892) or YFP-NLRP3 and then challenged with an i.p. injection of MSU crystals for 16 h (bottom). *n*= 7-11 mice, each one represented by a dot; Mann-Whitney test.

(**B**) CXCL1, CXCL10 and CCL2 chemokines in the peritoneal lavage of *Nlrp3*$^{-/-}$ mice treated as in (A). *n*= 8-11 mice, each one represented by a dot; Mann-Whitney test.

(**C**) Quantification of CD11b^{+}, Ly6G^{+} and F4/80^{-} cells in the peritoneal lavage of *Nlrp3*$^{-/-}$ mice treated as in (A). *n*= 5-11 mice, each one represented by a dot; Mann-Whitney test.

Figure 1

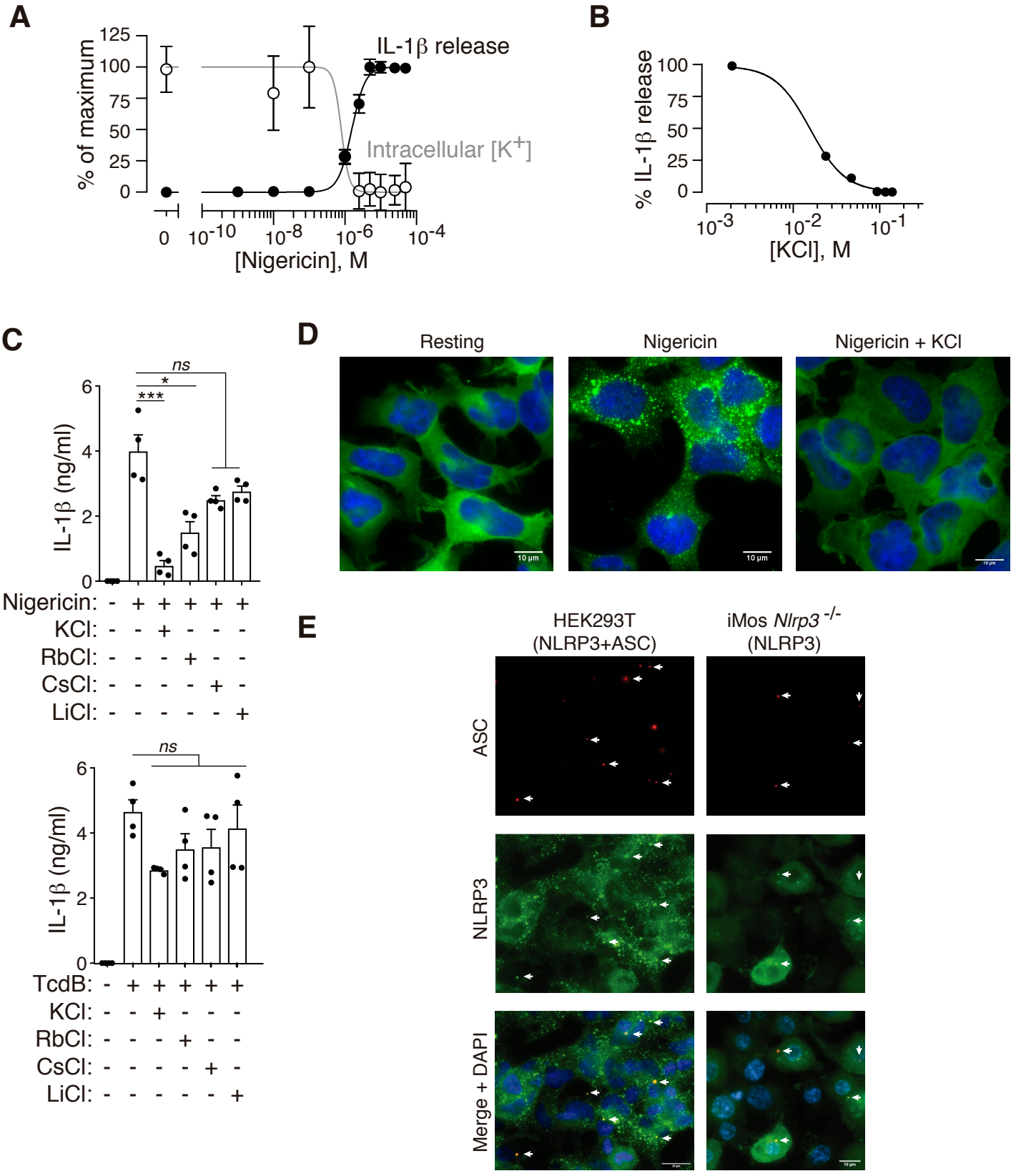
A
% of maximum
125
100
75
50
25
0
IL-1β release
Intracellular [K+]
0
10-10
10-8
10-6
10-4
[Nigericin], M
B
% IL-1β release
100
75
50
25
0
10-3
10-2
10-1
[KCl], M
C
IL-1β (ng/ml)
ns
*
***
Nigericin: - + + + + +
KCl: - - + - - -
RbCl: - - - + - -
CsCl: - - - - + -
LiCl: - - - - - +
TcdB: - + + + + +
D
Resting
Nigericin
Nigericin + KCl
10 µm
E
HEK293T
(NLRP3+ASC)
iMos Nlrp3 -/-
(NLRP3)
ASC
NLRP3
Merge + DAPI

Figure 2

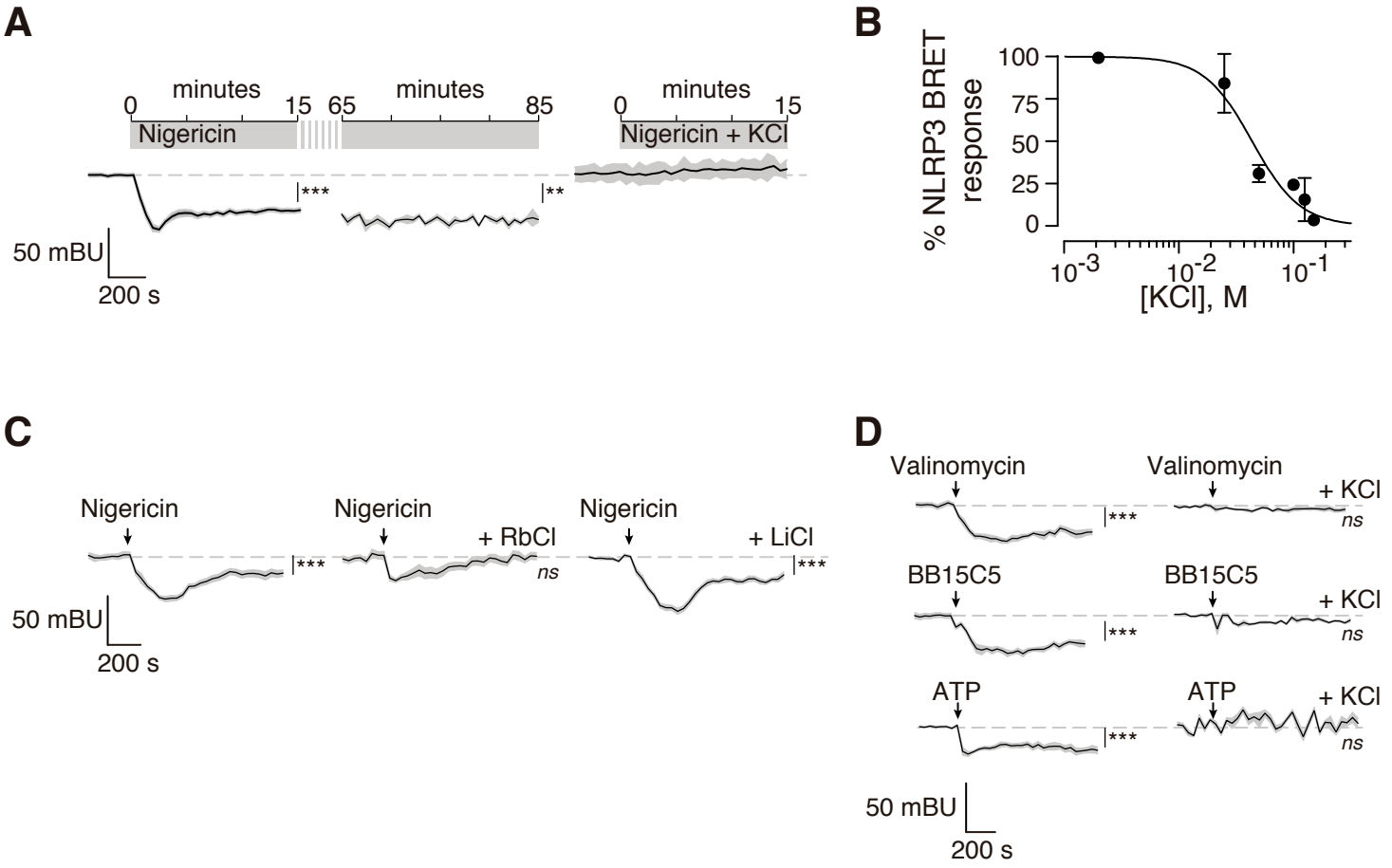
A
minutes
0
15
65
minutes
85
0
minutes
15
Nigericin
Nigericin + KCl
***
**
50 mBU
200 s
B
% NLRP3 BRET response
100
75
50
25
0
10-3
10-2
10-1
[KCl], M
C
Nigericin
Nigericin
+ RbCl
Nigericin
+ LiCl
***
ns
***
50 mBU
200 s
D
Valinomycin
Valinomycin
+ KCl
***
ns
BB15C5
BB15C5
+ KCl
***
ns
ATP
ATP
+ KCl
***
ns
50 mBU
200 s

Figure 3

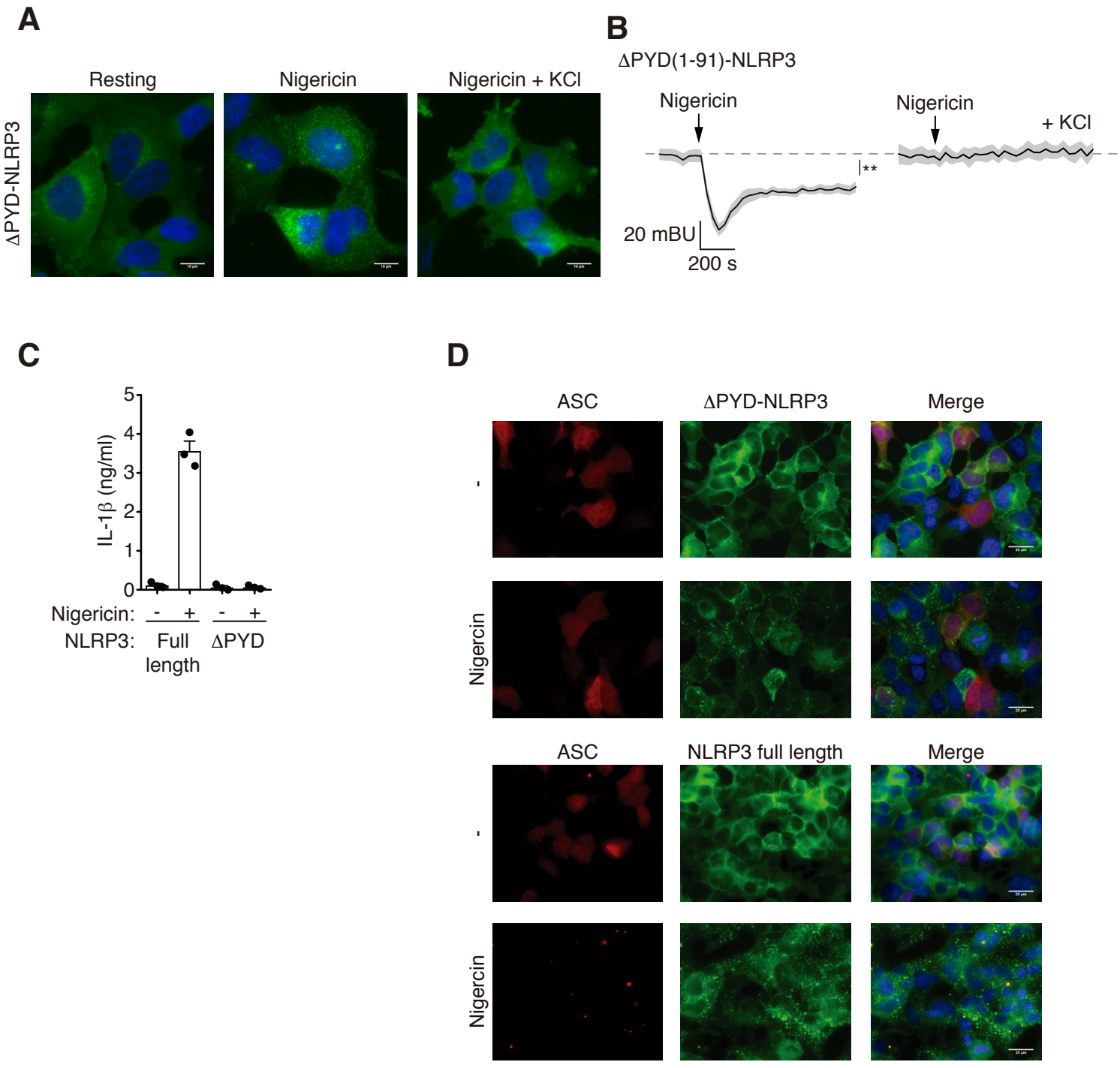
A
Resting
Nigericin
Nigericin + KCl
ΔPYD-NLRP3
B
ΔPYD(1-91)-NLRP3
Nigericin
Nigericin
+ KCl
**
20 mBU
200 s
C
IL-1β (ng/ml)
0
1
2
3
4
5
Nigericin: - + - +
NLRP3: Full length ΔPYD
D
ASC
ΔPYD-NLRP3
Merge
-
Nigercin
ASC
NLRP3 full length
Merge
-
Nigercin

Figure 4

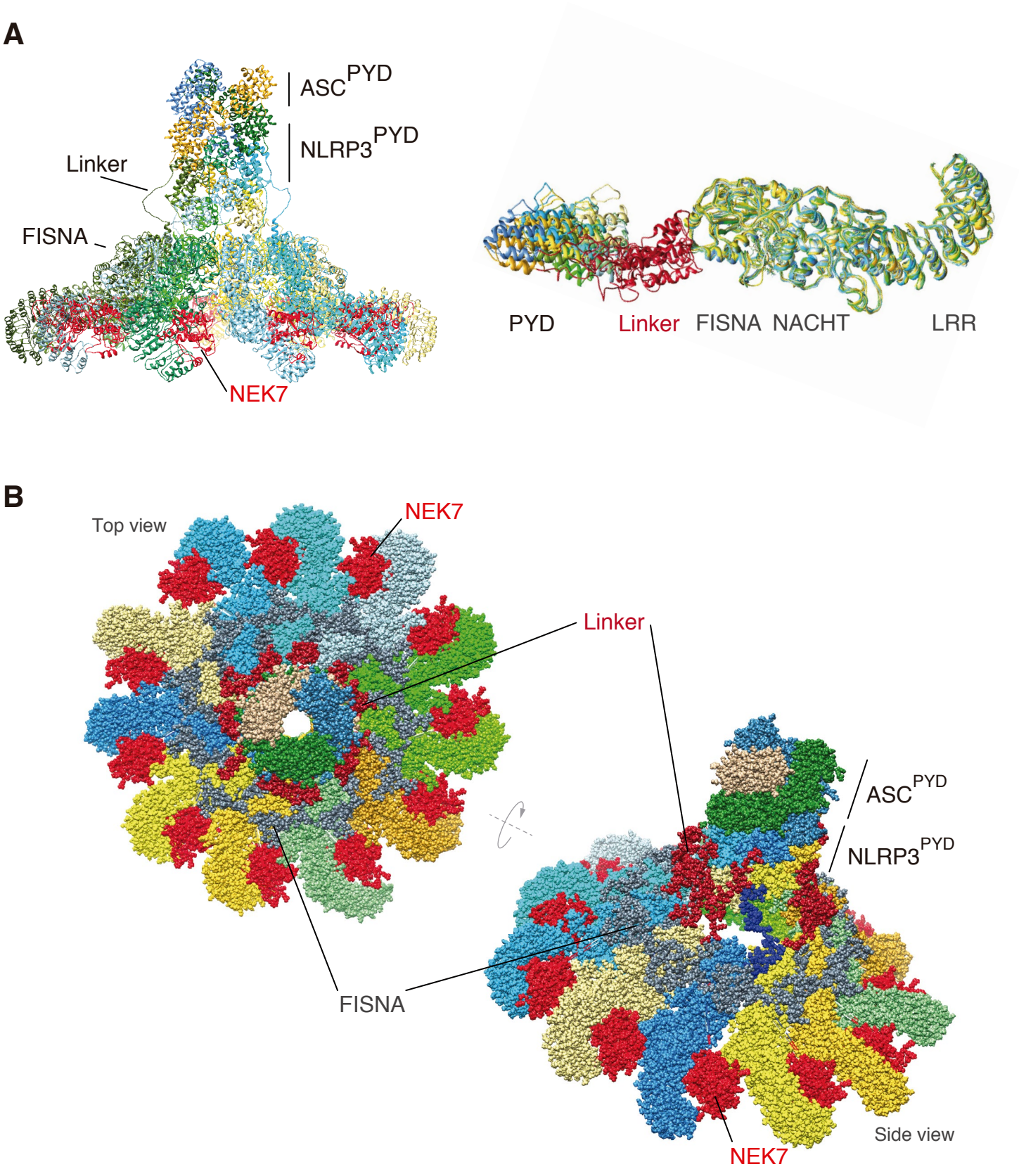
A
ASC^PYD
NLRP3^PYD
Linker
FISNA
NEK7
PYD
Linker
FISNA
NACHT
LRR
B
Top view
NEK7
Linker
FISNA
ASC^PYD
NLRP3^PYD
NEK7
Side view

Figure 5

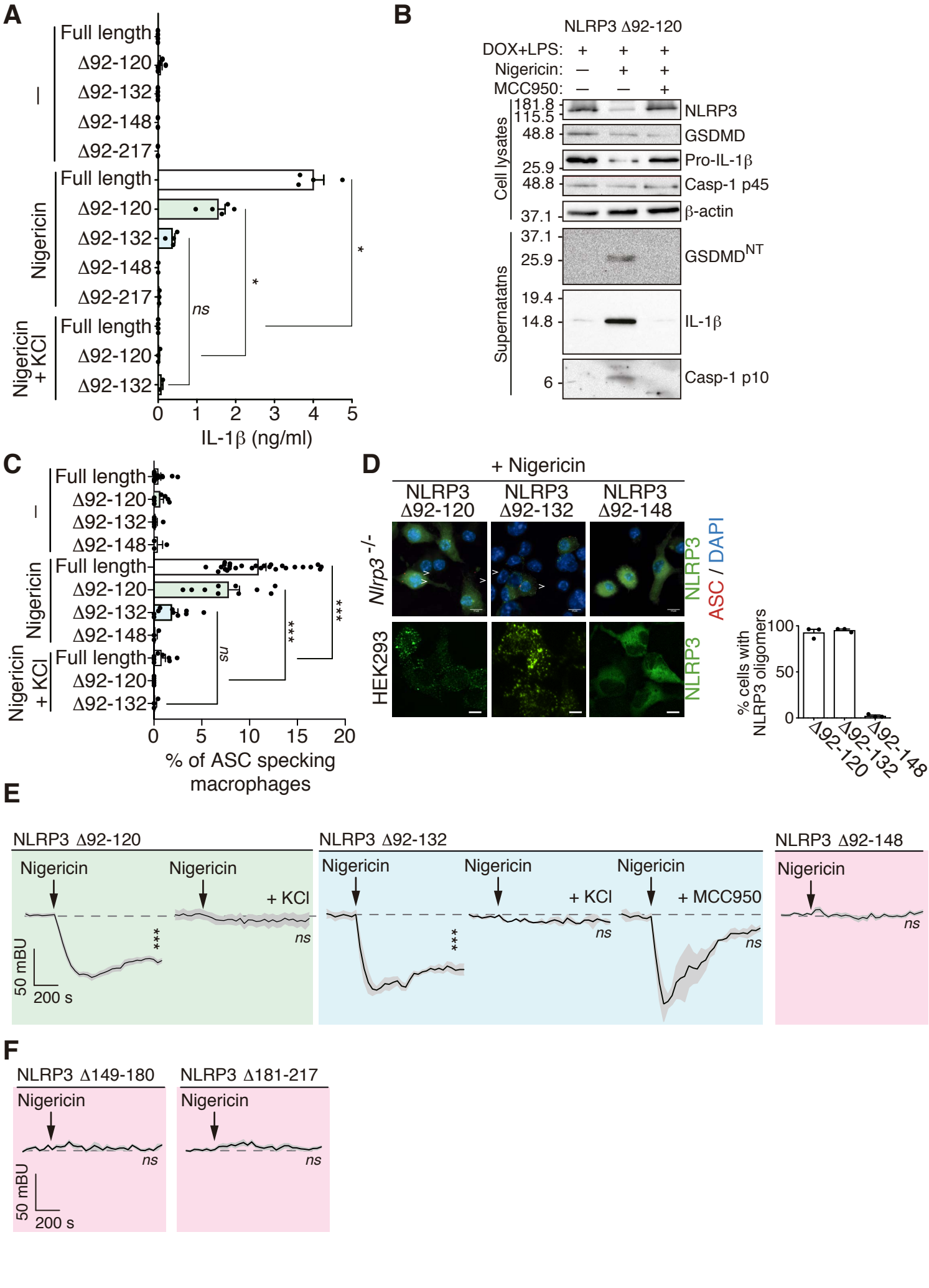
A
Full length
Δ92-120
Δ92-132
Δ92-148
Δ92-217
–
Nigericin
Nigericin + KCl
ns
*
IL-1β (ng/ml)
B
NLRP3 Δ92-120
DOX+LPS:
Nigericin:
MCC950:
Cell lysates
Supernatatns
NLRP3
GSDMD
Pro-IL-1β
Casp-1 p45
β-actin
GSDMD^NT
IL-1β
Casp-1 p10
C
***
su
% of ASC specking macrophages
D
+ Nigericin
NLRP3 Δ92-120
NLRP3 Δ92-132
NLRP3 Δ92-148
Nlrp3 -/-
HEK293
NLRP3
ASC / DAPI
% cells with NLRP3 oligomers
E
NLRP3 Δ92-120
NLRP3 Δ92-132
NLRP3 Δ92-148
Nigericin
+ KCl
+ MCC950
50 mBU
200 s
F
NLRP3 Δ149-180
NLRP3 Δ181-217

Figure 6

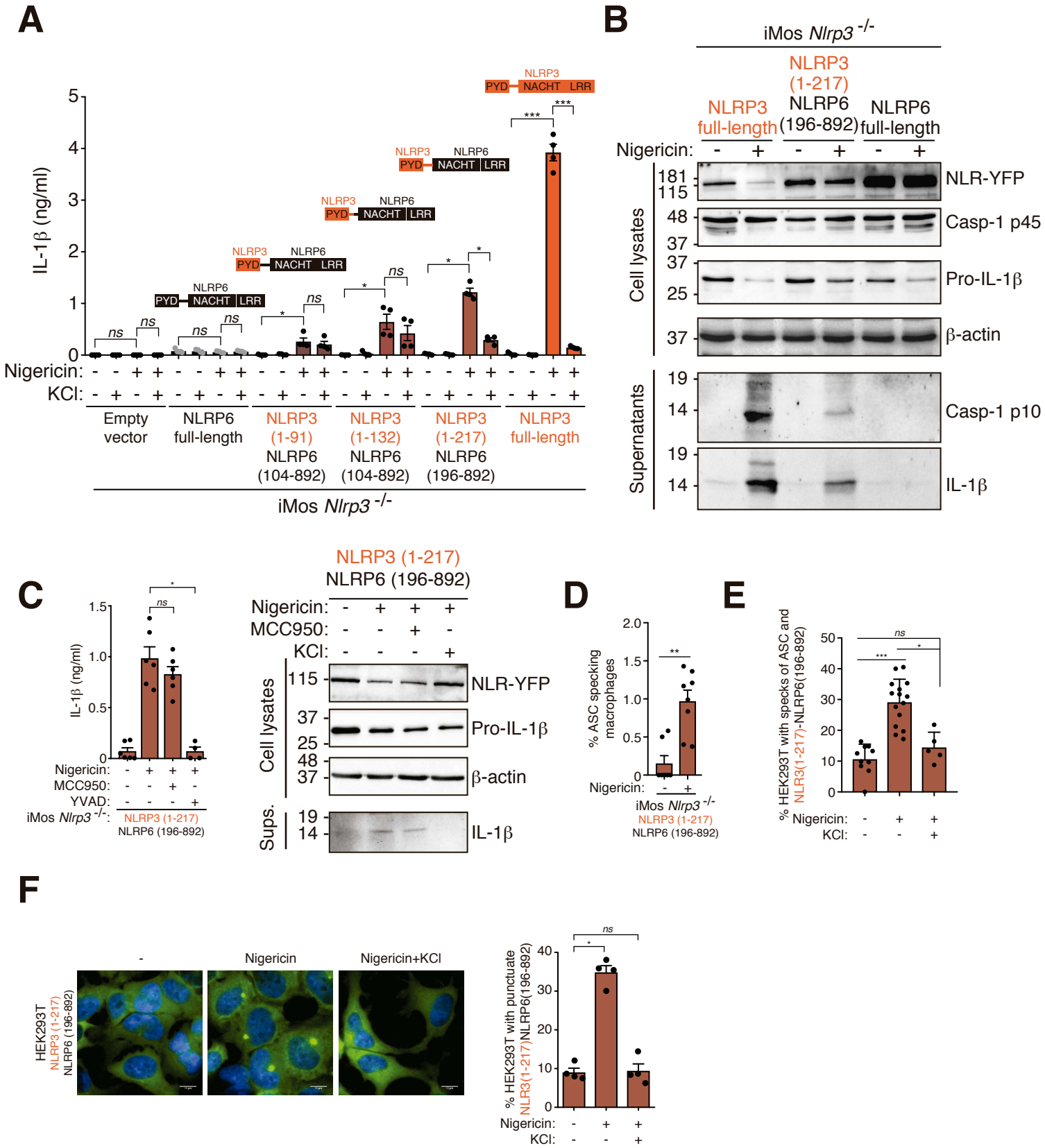
A
IL-1β (ng/ml)
Nigericin:
KCl:
Empty vector
NLRP6 full-length
NLRP3 (1-91) NLRP6 (104-892)
NLRP3 (1-132) NLRP6 (104-892)
NLRP3 (1-217) NLRP6 (196-892)
NLRP3 full-length
iMos Nlrp3 -/-
B
iMos Nlrp3 -/-
NLRP3 full-length
NLRP3 (1-217) NLRP6 (196-892)
NLRP6 full-length
Nigericin:
Cell lysates
Supernatants
NLR-YFP
Casp-1 p45
Pro-IL-1β
β-actin
Casp-1 p10
IL-1β
C
IL-1β (ng/ml)
Nigericin:
MCC950:
YVAD:
iMos Nlrp3 -/-:
NLRP3 (1-217) NLRP6 (196-892)
NLRP3 (1-217) NLRP6 (196-892)
Nigericin:
MCC950:
KCl:
Cell lysates
Sups.
NLR-YFP
Pro-IL-1β
β-actin
IL-1β
D
% ASC specking macrophages
Nigericin:
iMos Nlrp3 -/-
NLRP3 (1-217) NLRP6 (196-892)
E
% HEK293T with specks of ASC and NLR3(1-217)-NLRP6(196-892)
Nigericin:
KCl:
F
HEK293T NLRP3 (1-217) NLRP6 (196-892)
-
Nigericin
Nigericin+KCl
% HEK293T with punctuate NLR3(1-217)/NLRP6(196-892)
Nigericin:
KCl:

Figure 7

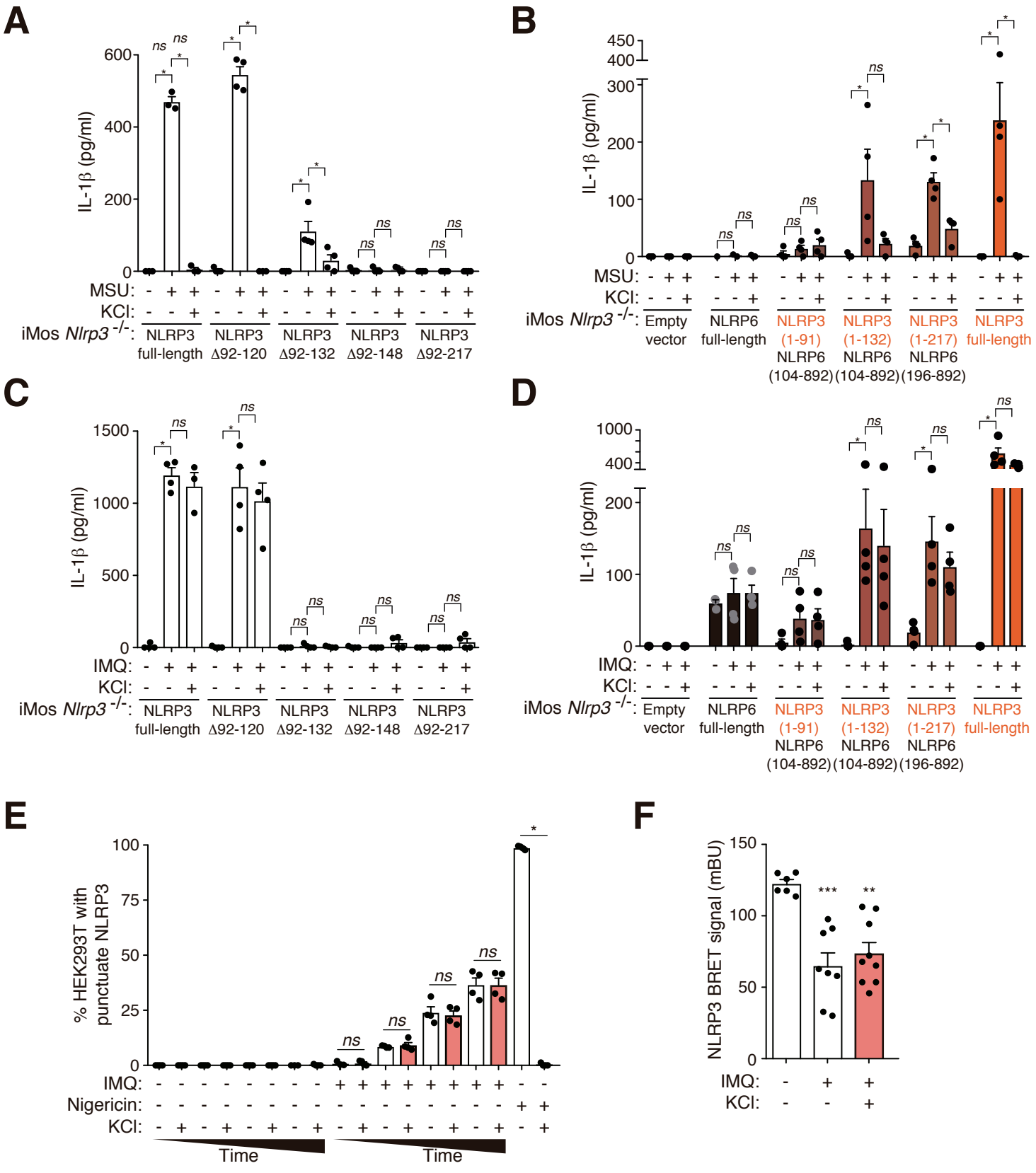
A
IL-1β (pg/ml)
MSU:
KCl:
iMos Nlrp3 -/-:
NLRP3 full-length
NLRP3 Δ92-120
NLRP3 Δ92-132
NLRP3 Δ92-148
NLRP3 Δ92-217
B
IL-1β (pg/ml)
MSU:
KCl:
iMos Nlrp3 -/-:
Empty vector
NLRP6 full-length
NLRP3 (1-91) NLRP6 (104-892)
NLRP3 (1-132) NLRP6 (104-892)
NLRP3 (1-217) NLRP6 (196-892)
NLRP3 full-length
C
IL-1β (pg/ml)
IMQ:
KCl:
iMos Nlrp3 -/-:
NLRP3 full-length
NLRP3 Δ92-120
NLRP3 Δ92-132
NLRP3 Δ92-148
NLRP3 Δ92-217
D
IL-1β (pg/ml)
IMQ:
KCl:
iMos Nlrp3 -/-:
Empty vector
NLRP6 full-length
NLRP3 (1-91) NLRP6 (104-892)
NLRP3 (1-132) NLRP6 (104-892)
NLRP3 (1-217) NLRP6 (196-892)
NLRP3 full-length
E
% HEK293T with punctuate NLRP3
IMQ:
Nigericin:
KCl:
Time
Time
F
NLRP3 BRET signal (mBU)
IMQ:
KCl:

Figure 8

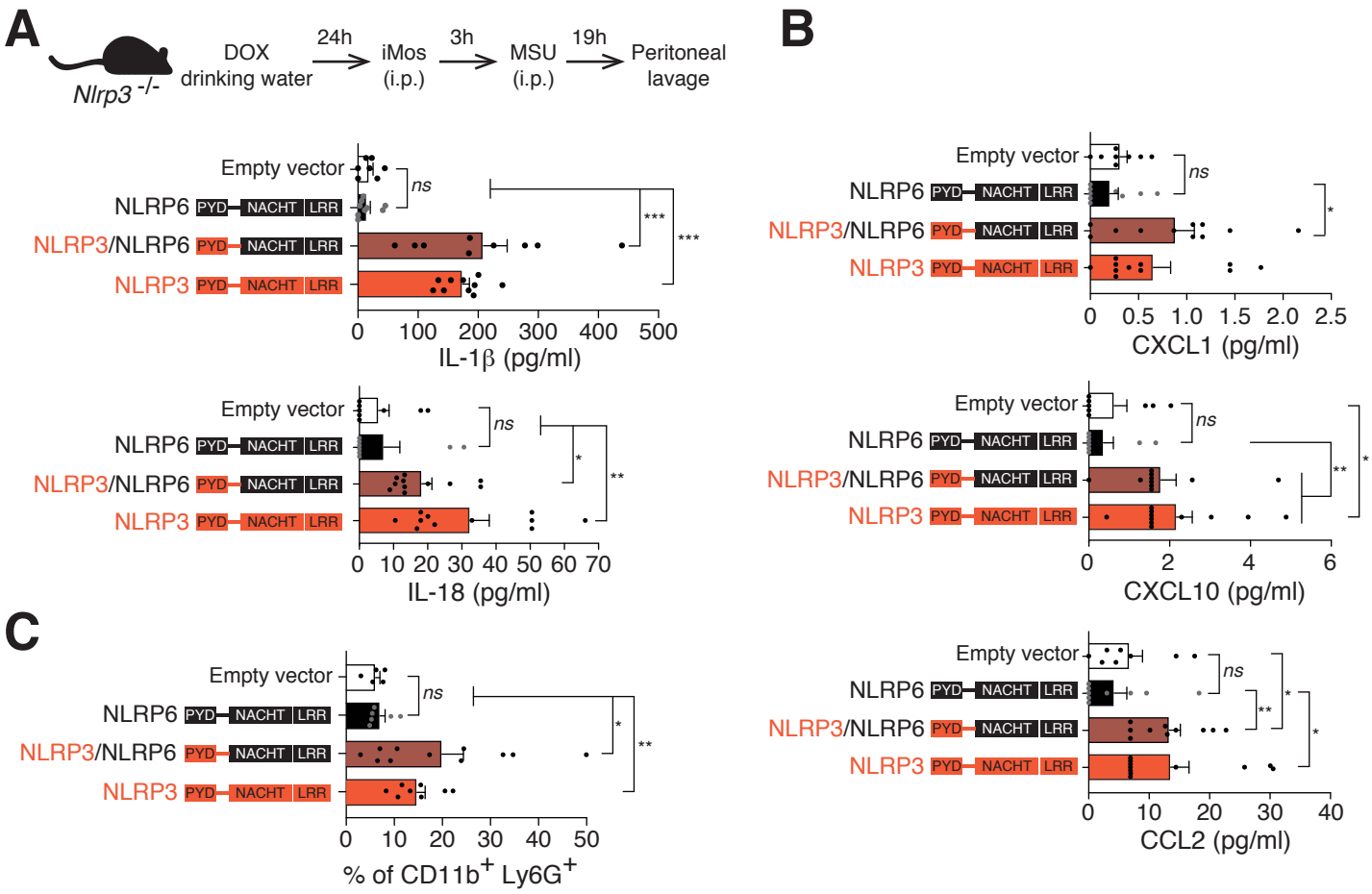
A
Nlrp3 -/-
DOX
drinking water
24h
iMos
(i.p.)
3h
MSU
(i.p.)
19h
Peritoneal
lavage
Empty vector
NLRP6
NLRP3/NLRP6
NLRP3
PYD
NACHT
LRR
ns
***
IL-1β (pg/ml)
0 100 200 300 400 500
*
**
IL-18 (pg/ml)
0 10 20 30 40 50 60 70
B
CXCL1 (pg/ml)
0 0.5 1.0 1.5 2.0 2.5
CXCL10 (pg/ml)
0 2 4 6
CCL2 (pg/ml)
0 10 20 30 40
C
% of CD11b+ Ly6G+
0 10 20 30 40 50

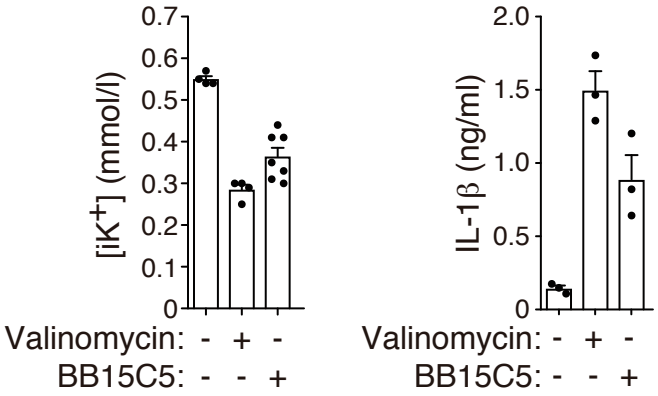

Figure S1. Intracellular K^+-efflux activates NLRP3.

Intracellular K^+ concentration ([iK^+], left) and IL-1β release (right) from LPS-primed bone marrow derived macrophages (BMDM) activated for 2 h with different K^+ ionophores (50 μM); *n*= 4-7 independent experiments for intracellular K^+; *n*= 3 independent experiments for IL-1β.

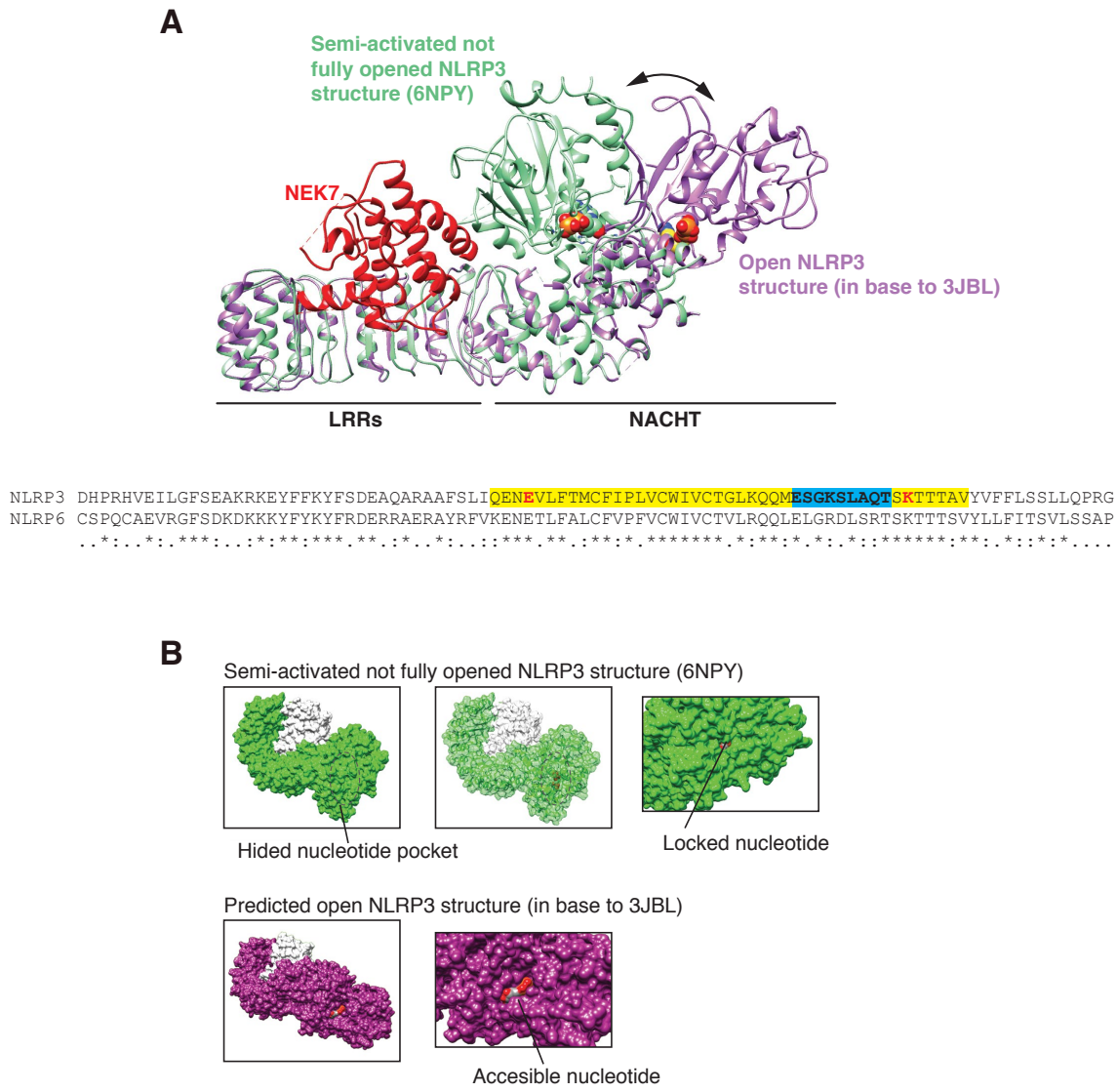

Figure S2. A closed NLRP3 structure presents a shielded nucleotide binding pocket.

(**A**) Model showing a semi-activated not fully opened (green) and open (magenta) NLRP3 structure (top). Clustal alignment of HD1 motif from human NLRP3 and NLRP6, denoting in cyan the hinge loop, in yellow the two helix motion, and with red annotation the residues E^{401} and K^{435} that present H-bond (bottom).

(**B**) Modeled semi-activated not fully opened (green) and open (magenta) NLRP3 structure showing the accessibility of the nucleotide binding pocket for both models. In the closed structure the nucleotide is locked in a hided nucleotide binding pocket.

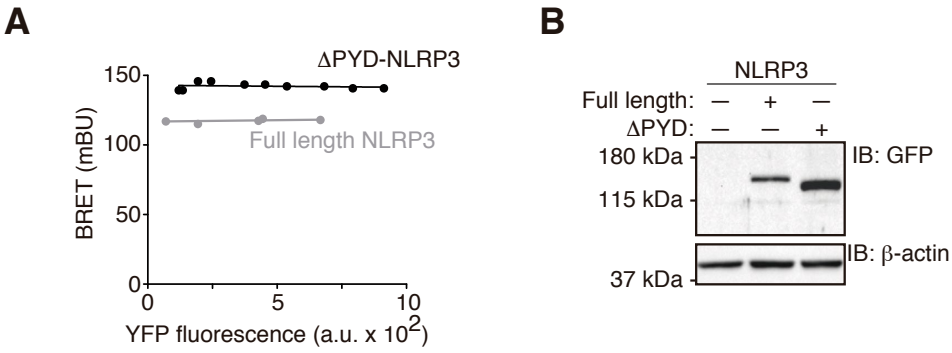

Figure S3. NLRP3 PYD domain is not necessary for NLRP3 oligomerization, but is required to form active NLRP3 oligomers.

(**A**) BRET signal of increasing amounts of YFP-ΔPYD-NLRP3-Luc or YFP-NLRP3-Luc expressed in HEK293T cells plotted as a function of the amount of protein. Resulting BRET signal is due to intramolecular energy transfer. As expected for intramolecular energy transfer, BRET does not increase in cells expressing higher amounts of sensor. *n*= 2 independent experiments for each construction and expression level.

(**B**) Western blot for GFP (detecting YFP-NLRP3 and YFP-ΔPYD-NLRP3) and β-actin from cell lysates of *Nlrp3*$^{-/-}$ immortalized macrophages (iMos) treated for 16 h with doxycycline (1 μg/ml) and LPS (100 ng/ml); representative of *n*= 2 independent experiments.

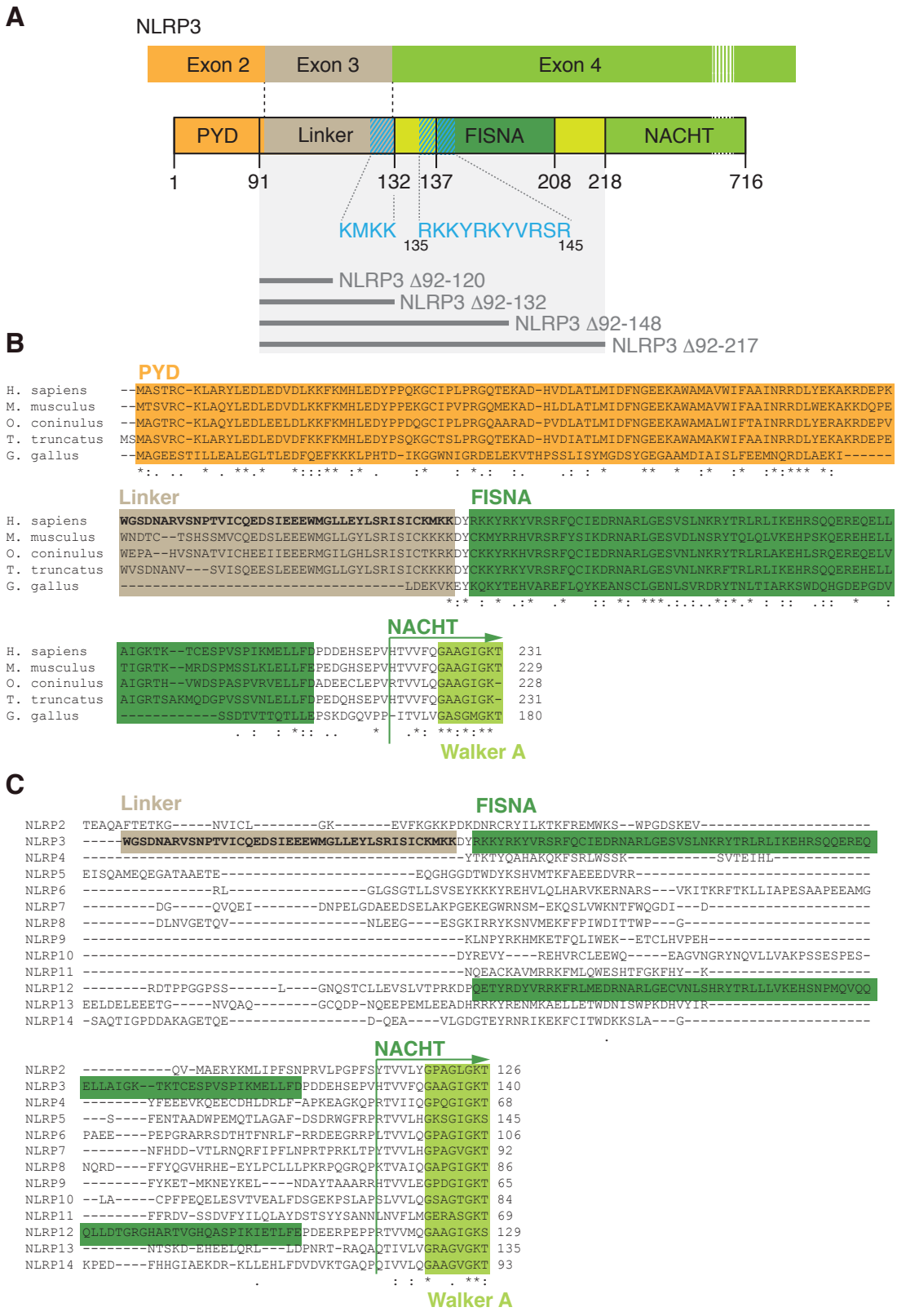

Figure S4. NLRP3 N-terminus sequence features.

(**A**) Scheme representation of NLRP3 for the first four exons and the different domains of the NLRP3 protein. In blue are highlighted the two polybasic sequences. The grey bars at the bottom of the panel represent the different NLRP3 truncations used in this study.

(**B**) Clustal Omega multi-alignment of the N-terminal protein sequences for NLRP3 form different species. PYD domain is highlighted in orange, linker sequence is highlighted in brown, the FISNA domain is highlighted in dark green and the Walker A motif in the NACHT domain is highlighted in light green.

(**C**) Clustal Omega multi-alignment of the protein sequences between PYD domain and the Walker A motif in the NACHT domain for the different human NLRPs. The NLRP3 linker sequence is highlighted in brown, the FISNA domain is highlighted in dark green and the Walker A motif in the NACHT domain is highlighted in light green.

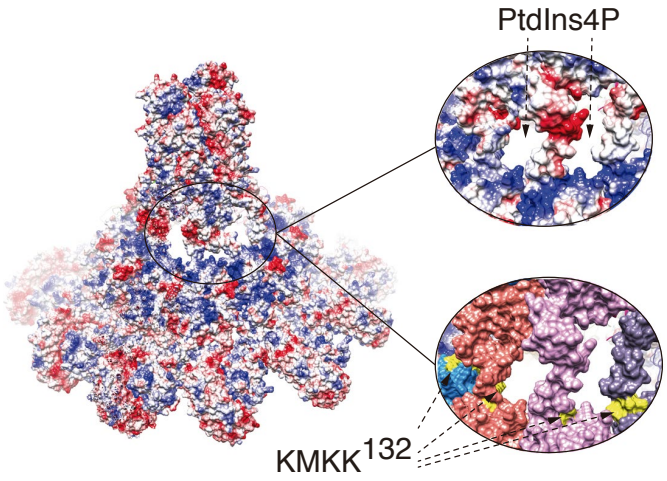

Figure S5. Model of ASC^{PYD}-NLRP3-NEK7 oligomer.

Detail of the electrostatic field surface of the oligomer showing the linker sequence. Negatively charged electrostatic field is shown in red and positively charged in blue (hue from red to blue shows the strength of the field). The surface is calculated as the solvent accessible surface of two interacting monomers of NLRP3 of the inflammasome complex. The empty space between the linkers of both monomers shows a putative location for a PtdIns4P molecule binding. Polybasic KMKK^{132} sequence is highlighted in yellow in the magnification.

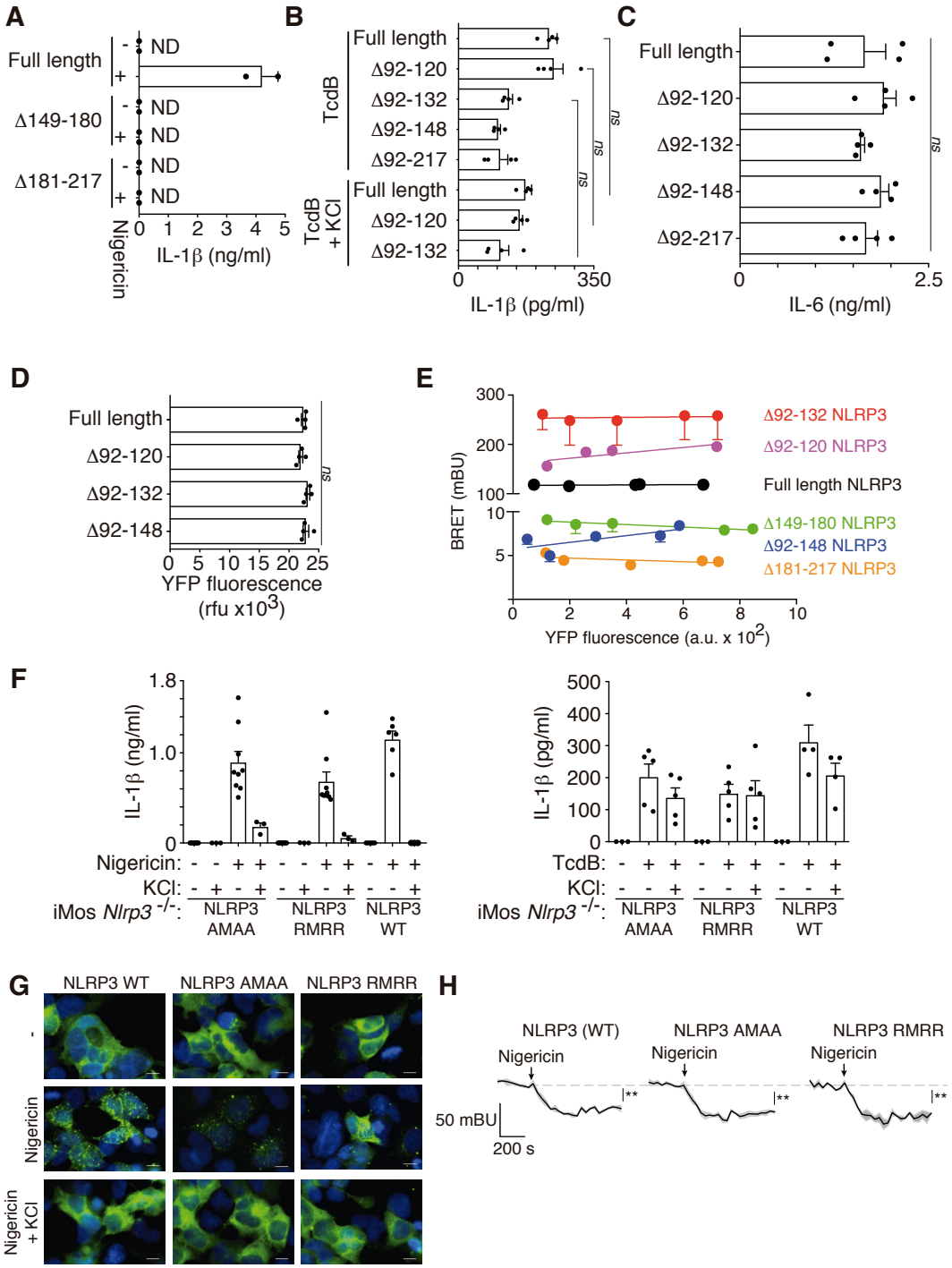

Figure S6. NLRP3 linker and FISNA domain in inflammasome activation.

(**A**) IL-1β release from *Nlrp3*$^{-/-}$ immortalized macrophages (iMos) treated for 16 h with doxycycline (1 μg/ml) and LPS (100 ng/ml) to induce the expression of different YFP-NLRP3 truncations as indicated and then activated for 60 min with nigericin (10 μM). *n*= 2 independent experiments.

(**B**) IL-1β release from *Nlrp3*$^{-/-}$ iMos treated for 16h with doxycycline (1 μg/ml) and LPS (100 ng/ml) to induce the expression of different YFP-NLRP3 truncations as indicated and then activated for 60 min with the *C. difficile* toxin B (TcdB, 1 μg/ml) in the absence/presence of 40 mM KCl. *n*= 4 independent experiments; Kruskal-Wallis test.

(**C**) IL-6 release from *Nlrp3*$^{-/-}$ iMos treated for 16h with doxycycline (1 μg/ml) and LPS (100 ng/ml) to induce the expression of different YFP-NLRP3 truncations as indicated. *n*= 4 independent experiments; Kruskal-Wallis test.

(**D**) YFP fluorescence of HEK293T cells expressing YFP-NLRP3-Luc, YFP-Δ92-120-NLRP3-Luc, YFP-Δ92-132-NLRP3-Luc and YFP-Δ92-148-NLRP3-Luc. *n*= 4 independent experiments.

(**E**) BRET signal of increasing amounts of full length and different deletions of NLRP3 (as indicated) tagged at N-terminal with YFP and at C-terminal with Luc expressed in HEK293T cells plotted as a function of the amount of protein. Resulting BRET signal for the different deletions is due to intramolecular energy transfer. As expected for intramolecular energy transfer, BRET does not proportionally increase in cells expressing higher amounts of sensor. *n*= 2 independent experiments for each construction and expression level.

(**F**) IL-1β release from *Nlrp3*$^{-/-}$ iMos treated as in (A) expressing YFP-NLRP3 wild-type, AMAA^{132} or RMRR^{132} mutations and activated after priming for 60 min with nigericin (10 μM) or TcdB (1 μg/ml) in the absence/presence of 40 mM KCl. *n*= 3-9 independent experiments.

(**G**) Representative fluorescent micrographs of HEK293 cells expressing YFP-NLRP3 wild-type, AMAA^{132} or RMRR^{132} mutations (green) and stained for nuclei (DAPI, blue) treated for 30 min with nigericin (10 μM) in the absence/presence of 140 mM KCl. Scale bar 10 μm.

(**H**) Average BRET signal for YFP-NLRP3-Luc, YFP-AMAA^{132}-NLRP3-Luc and YFP-RMRR^{132}-NLRP3-Luc expressed in HEK293T cells before and after stimulation with nigericin (10 μM, added when denoted by an arrow); please note kinetics of BRET have been plotted with the same scale, but relatively at the same initial level to ease comparison. *n*= 2-4 independent experiments; Mann-Whitney test.

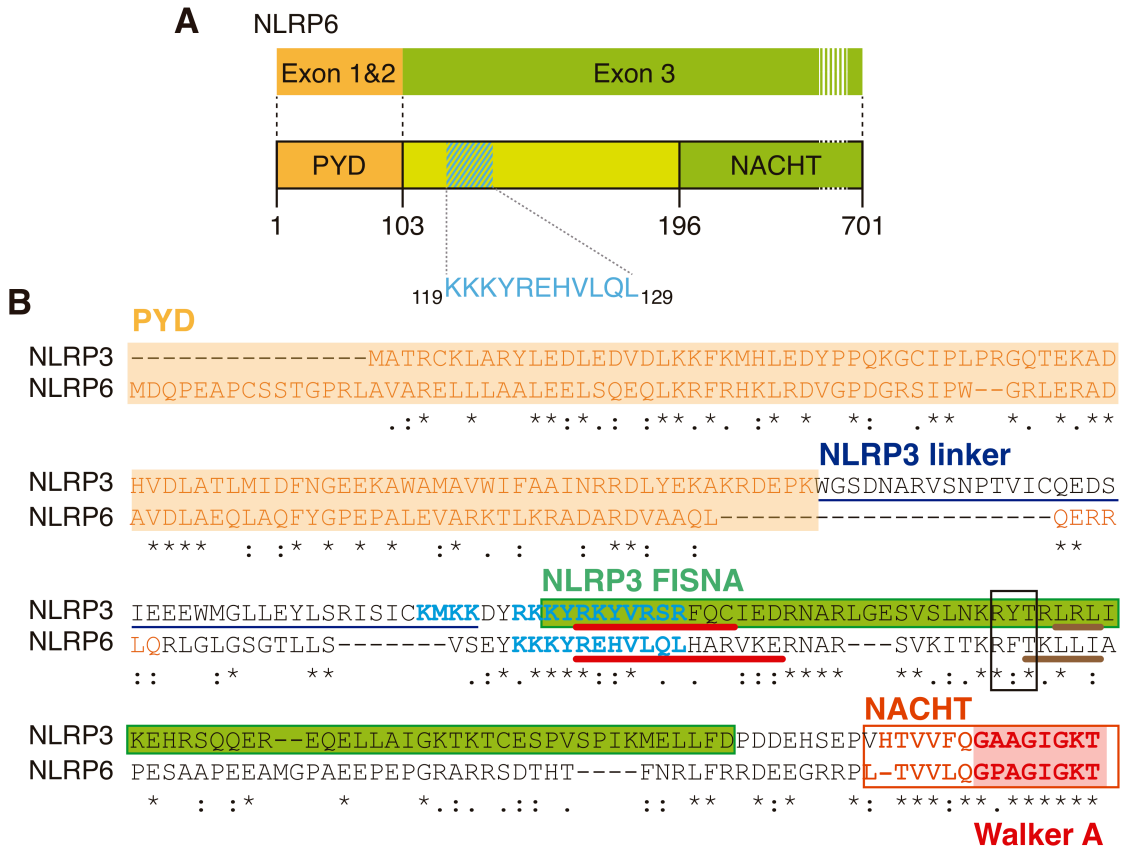

Figure S7. Comparison of the N-terminal sequence of NLRP3 and NLRP6.

(**A**) Scheme representation of NLRP6 for the first three exons and the different domains for NLRP6 protein. In blue is highlighted the conserved polybasic sequence with NLRP3.

(**B**) Clustal alignment of human N-terminal sequences of NLRP6 and NLRP3. PYD domain is highlighted in orange, NLRP3 linker sequence is underlined in dark blue, the NLRP3 FISNA domain is highlighted in green, the polybasic sequences are indicated in light blue, and the Walker A motif in the NACHT domain is highlighted in red. Note the similarities of the NLRP3 FISNA sequence with NLRP6: underlined in red is annotated a predicted α-helix and underlined in brown is annotated a predicted β-sheet; sharing 49.27% homologous amino acids with the signature of the FISNA domain (pbKpsL+p+applbEGssp.GppsbLNclYT-LYIsEthss.lspEHEVbQIEpscp.ssp-sslcsp-LFc), and conserving key amino acids possible interacting with the nucleotide (boxed in black).

(**C**) Key amino acids of NLRP3 FISNA (RYT^{167}) potentially involved in nucleotide binding. Ribbon plot of the nucleotide binding of NLRP3 in the closed conformation shown in 6NPY structure. The Walker A motif of the NACHT domain is highlighted in cyan.

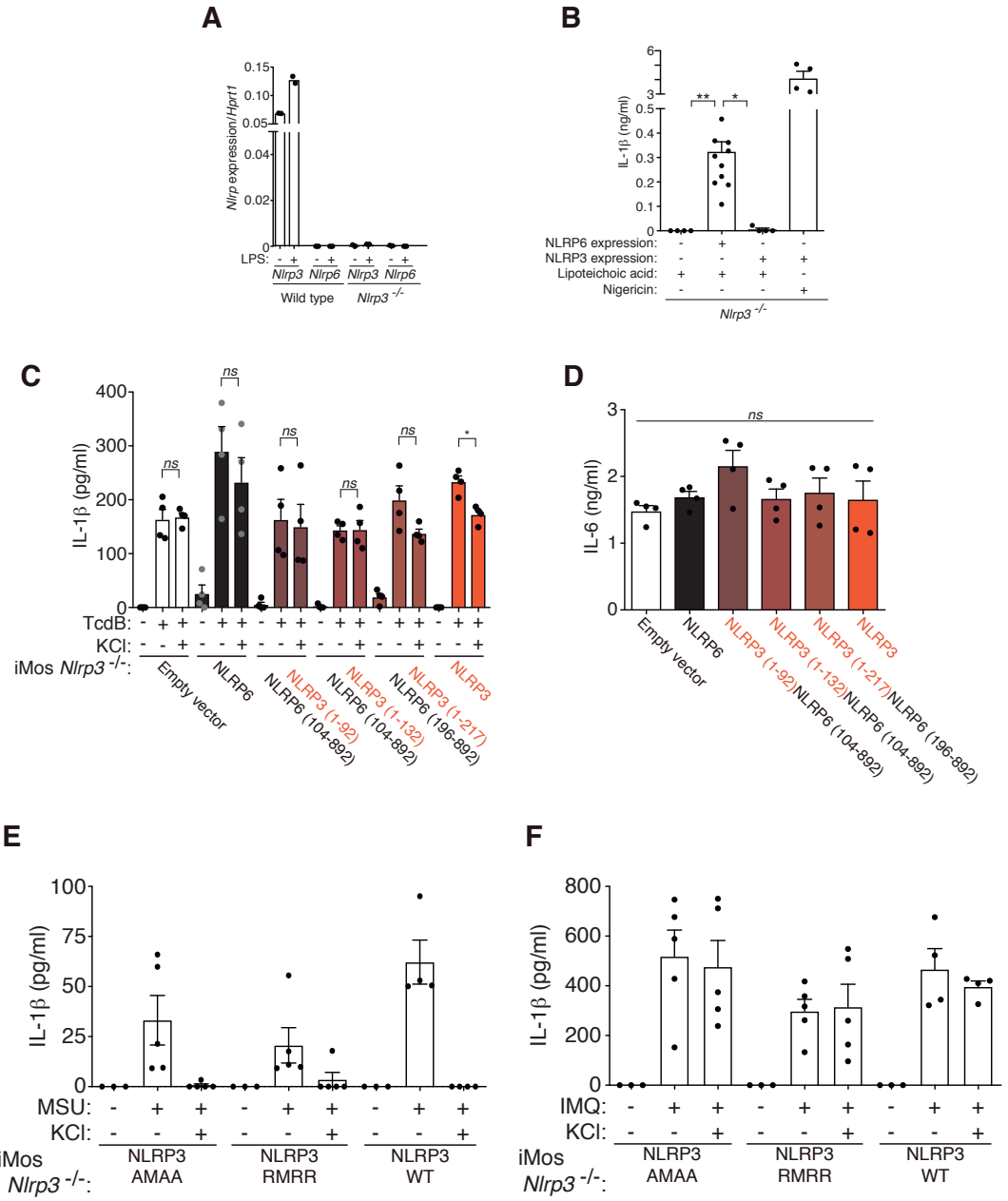

Figure S8. NLRP6 is not activated in response to K^+ efflux.

(**A**) Quantitative PCR for *Nlrp3* and *Nlrp6* expression from wild-type or *Nlrp3*$^{-/-}$ immortalized macrophages (iMos) treated for 16 h with or without LPS (100 ng/ml) as indicated; *n*= 2 independent experiments.

(**B**) IL-1β release from *Nlrp3*$^{-/-}$ immortalized macrophages (iMos) treated for 16 h with doxycycline (1 μg/ml) and lipoteichoic acid (15 μg/ml) to induce the expression of YFP-NLRP3 or YFP-NLRP6 as indicated, and activate NLRP6. As a positive control YFP-NLRP3 expressing macrophages were treated for 16 h with doxycycline (1 μg/ml) and LPS (100 ng/ml) and then activated for 60 min with nigericin (10 μM); *n*= 4-10 independent experiments; Kruskal-Wallis test.

(**C**) IL-1β release from *Nlrp3*$^{-/-}$ iMos treated for 16 h with doxycycline (1 μg/ml) and LPS (100 ng/ml) to prime and induce the expression of YFP-NLRP6, YFP-NLRP3 or different YFP-NLRP3/6 chimeric receptors as indicated and then activated for 60 min with the *C.*

difficile toxin B (TcdB, 1 μg/ml) in the absence/presence of 40 mM KCl; *n*= 4 independent experiments; Kruskal-Wallis test.

(**D**) IL-6 release from *Nlrp3*$^{-/-}$ iMos treated for 16 h with doxycycline (1 μg/ml) and LPS (100 ng/ml) to prime and induce the expression of different YFP-NLRP3/6 chimeric receptors as indicated; *n*= 4 independent experiments; Kruskal-Wallis test.

(**E**) IL-1β release from *Nlrp3*$^{-/-}$ immortalized macrophages (iMos) treated for 16h with doxycycline (1 μg/ml) and LPS (100 ng/ml) to induce the expression of YFP-NLRP3 AMAA^{132} or RMRR^{132} mutants as indicated and then activated for 16 h with MSU crystals (300 μg/ml) in the absence/presence of 40 mM KCl. *n*= 3-5 independent experiments.

(**F**) IL-1β release from *Nlrp3*$^{-/-}$ iMos treated for 16h with doxycycline (1 μg/ml) and LPS (100 ng/ml) to induce the expression of YFP-NLRP3 AMAA^{132} or RMRR^{132} mutants as indicated and then activated for 60 min with imiquimod (100 μM) in the absence/presence of 40 mM KCl. *n*= 3-5 independent experiments.

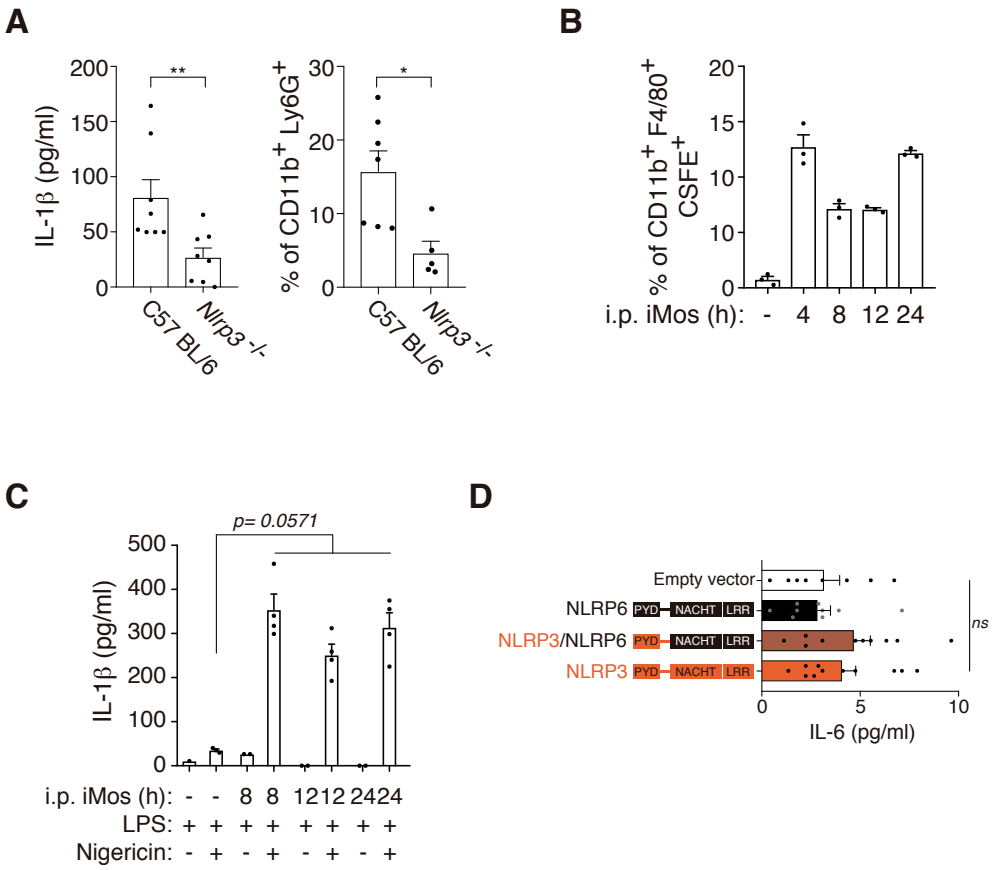

Figure S9. Reconstitution of *Nlrp3*$^{-/-}$ mice with macrophages expressing NLRP6 chimeric receptor harbouring the NLRP3 PYD-linker-FISNA.

(**A**) IL-1β and quantification of CD11b^{+}, Ly6G^{+} and F4/80^{-} cells in the peritoneal lavage of wild-type and *Nlrp3*$^{-/-}$ mice collected 16 h after i.p. injection of MSU crystals. *n*= 5-8 mice, each one represented by a dot; Mann-Whitney test.

(**B**) Percentage of immortalized macrophages (iMos) recovered from the peritoneal lavage of *Nlrp3*$^{-/-}$ mice after 4, 8, 12 and 24 h i.p. injection. iMos were stained with CFSE-FITC before injection and then stained also for CD11b and F4/80. *n*= 3 mice, each one represented by a dot.

(**C**) IL-1β release from *Nlrp3*$^{-/-}$ iMos expressing YFP-NLRP3 harvest from the peritoneum of mice after 8, 12 and 24 h after i.p. injection and then cultured *in vitro* for 4 h with LPS (1 μg/ml) and then activated for 30 min nigericin (10 μM). *n*= 1-4 mice, each one represented by a dot; Mann-Whitney test.

(**D**) IL-6 in the peritoneal lavage of *Nlrp3*$^{-/-}$ after an i.p. injection with *Nlrp3*$^{-/-}$ iMos expressing YFP-NLRP6, the chimera YFP-NLRP3(1-217)-NLRP6(196-892) or YFP-NLRP3 and then challenged with an i.p. injection of MSU crystals for 16 h; *n*= 8-11 mice, each one represented by a dot; Mann-Whitney test.

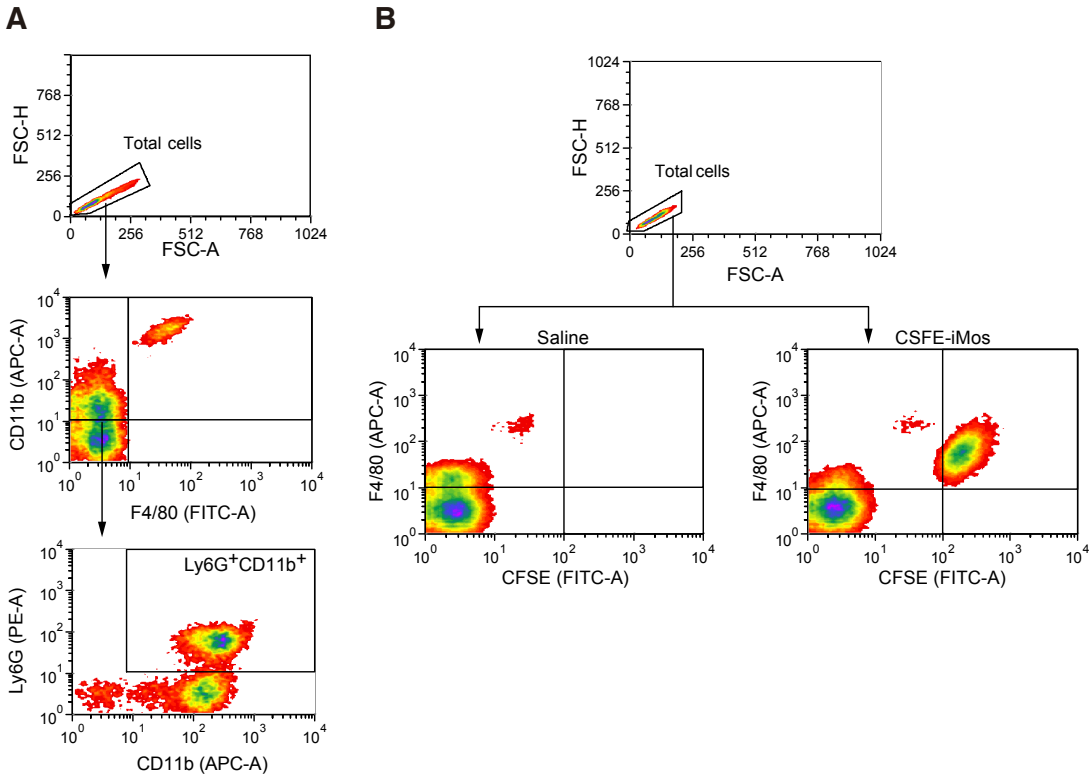

Figure S10. Flow cytometry gating strategy.
(**A**) Gating strategy of figure 8C. From total cells in FSC-H and FSC-A, cells were first gated for CD11b-APC and F4/80-FITC, then cells CD11b$^+$ and F4/80$^-$ were gated for Ly6G-PE and CD11b-APC to select Ly6G$^+$ and CD11b$^+$ cells shown in the figure.
(**B**) Gating strategy of supplementary figure S9B, showing recovered peritoneal cells from a representative mice i.p. injected with saline solution (left) or CFSE labelled immortalized macrophages (right) for 24 h.

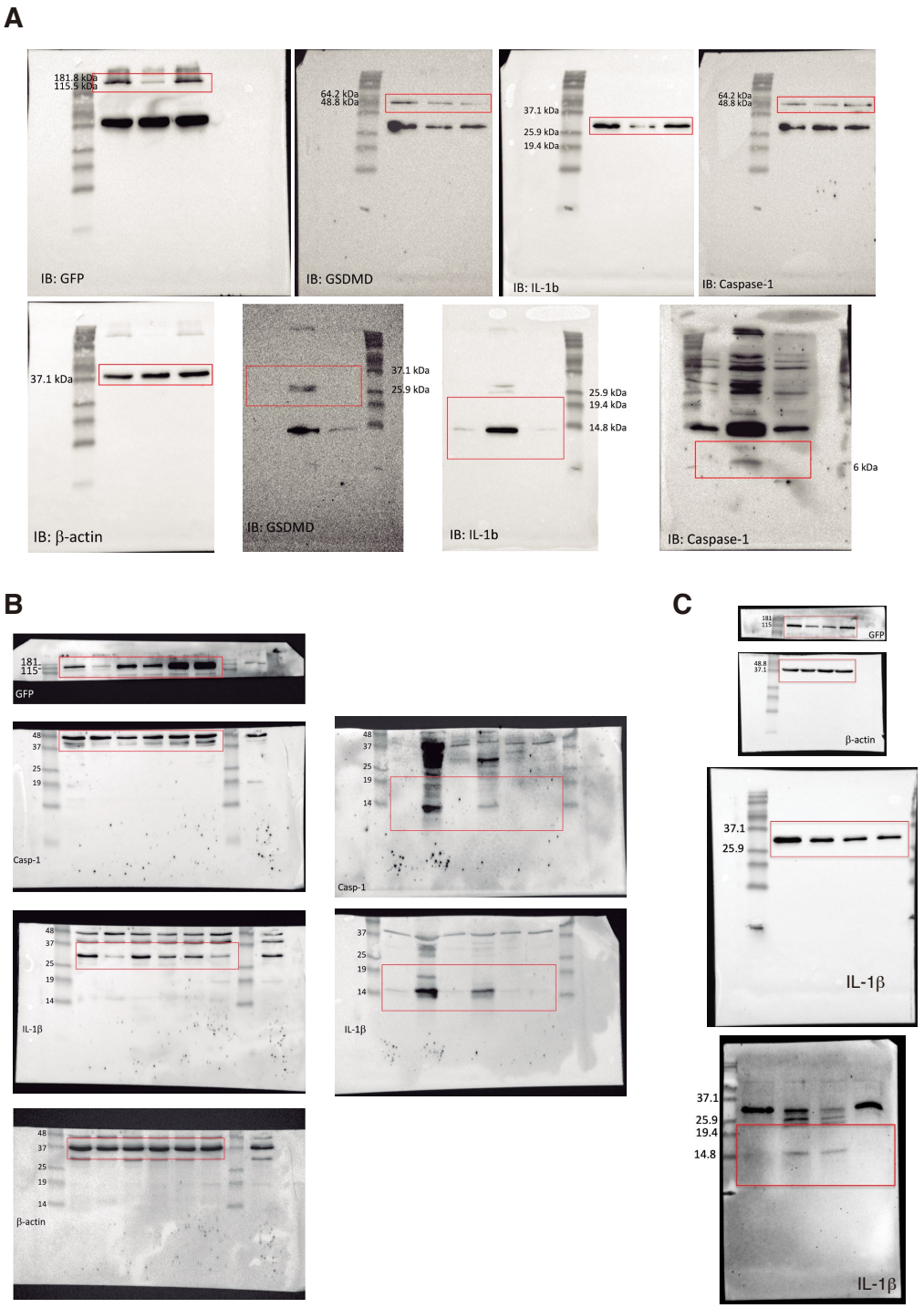

Figure S11. Uncropped Western blots of main figures.
(**A**) Uncropped Western blots of figure 5B.
(**B**) Uncropped Western blots of figure 6B.
(**C**) Uncropped Western blots of figure 6C.
For **A-C**, photo credit: Diego Angosto-Bazarra, Instituto Murciano de Investigación Biosanitaria IMIB-Arrixaca, Hospital Clínico Universitario Virgen de la Arrixaca, 30120 Murcia, Spain.

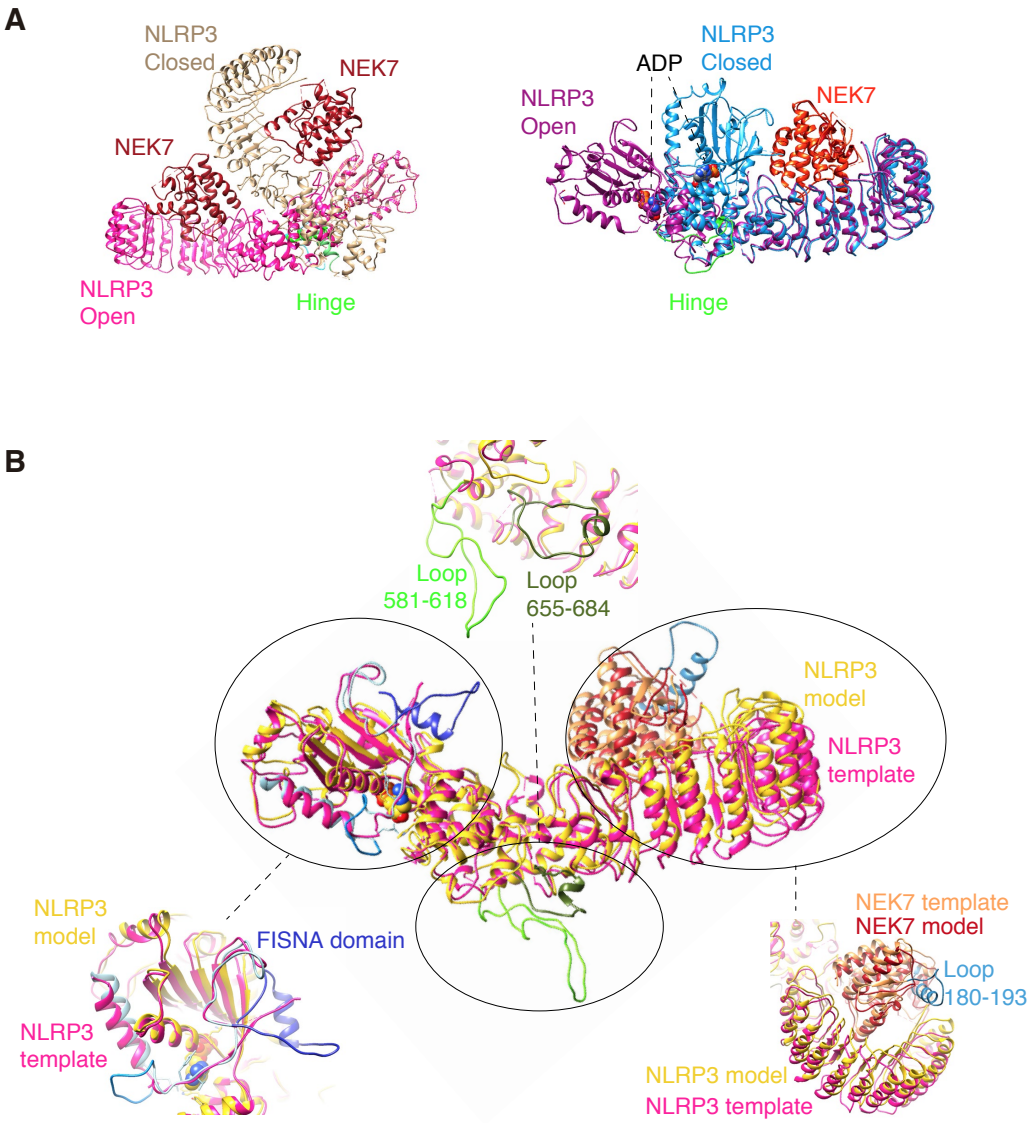

Figure S12. Model of NLRP3 monomer in open and closed conformation.
(**A**) Model of NLRP3 in open and closed conformation.
(**B**) Model of missing loops in the structure 6NPY that includes NLRP3 and NEK7.

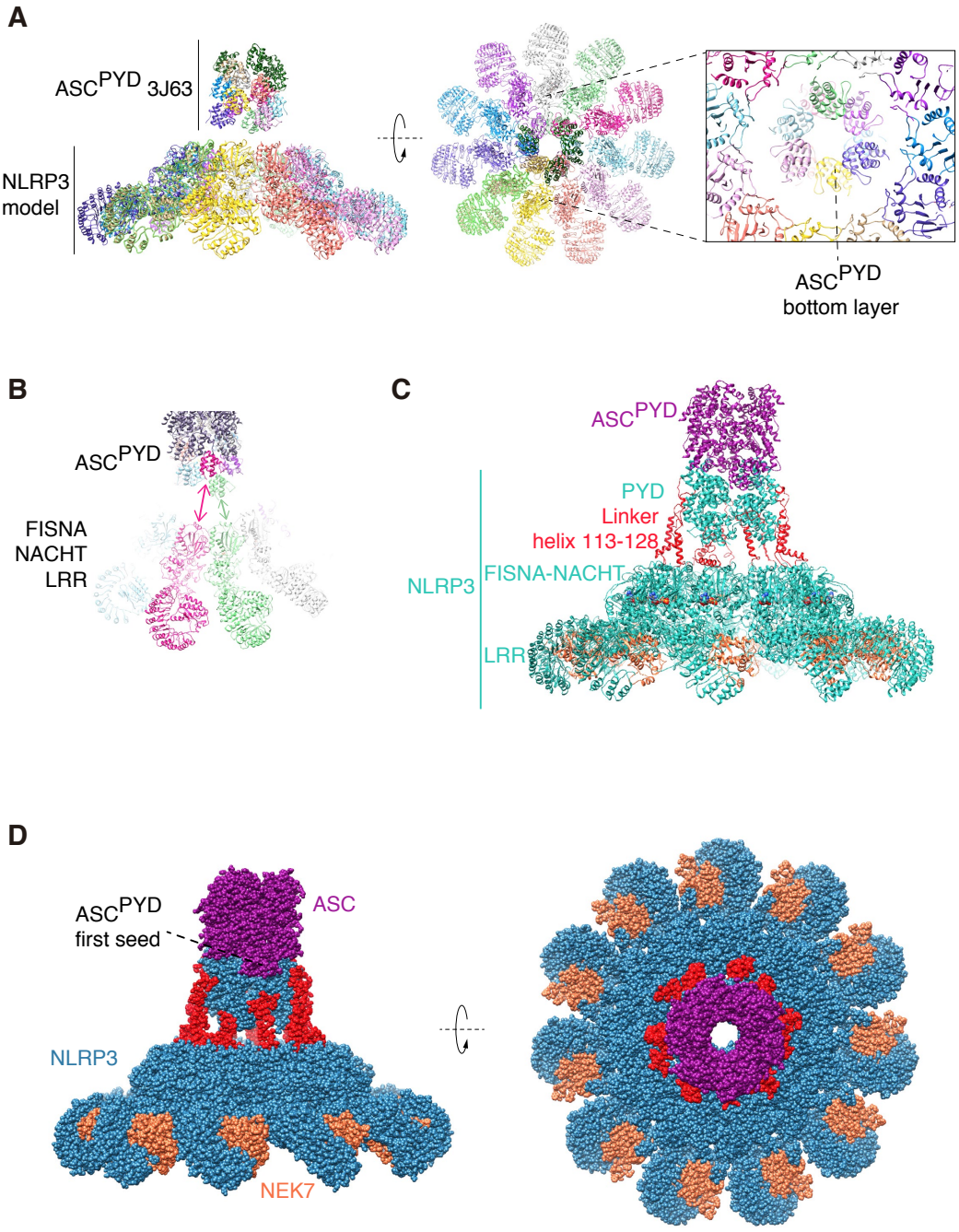

Figure S13. Modelling NLRP3 oligomer.
(**A**) A fiber of ASC^{PYD} (3J63) assembled near the N-terminus of the monomeric models of NLRP3 containing FISNA-NACHT-LRR preserving the symmetry of the complex. Insert shows the bottom layer of ASC^{PYD} from the fiber structure.
(**B**) Association of ASC^{PYD} chains from the bottom and next layer to each pair of close monomers of NLRP3.
(**C**) ASC^{PYD}-NLRP3-NEK7 complex formed by 13 ASC chains, 11 full chains of NLRP3 and 11 chains of NEK7. The structure of the NLRP3 linker (in red) was modelled as a loop forcing a helix in position 113-128.
(**D**) The different symmetry between NLRP3/NEK7 (with a C_{11} rotation axis) and the fiber of ASC^{PYD} (with a C_6 rotation axis) leaved the starting position of a chain of ASC^{PYD} as a seed to continue forming the ASC^{PYD} fiber.